Lipid tracking at kilohertz sampling rates on live cell membranes through Interferometric Scattering microscopy

Authors

Francesco Reina[1,2], Christian Eggeling[1,2,3,4], B. Christoffer Lagerholm[4]

[1]Leibniz-Institut für Photonische Technologien e.V., Jena 07745, Germany
[2]Institute of Applied Optics and Biophysics, Friedrich Schiller University Jena, Jena 07737, Germany
[3]MRC Human Immunology Unit, MRC Weatherall institute of Molecular Medicine, John Radcliffe Hospital, University of Oxford, Oxford OX3 9DS, United Kingdom
[4]Wolfson Imaging Centre, MRC Weatherall institute of Molecular Medicine, John Radcliffe Hospital, University of Oxford, Oxford OX3 9DS, United Kingdom

Abstract

The lateral dynamics of lipids on the cellular membranes are one of the most challenging topics to study in membrane biophysics, needing simultaneously high spatial and temporal resolution. In this study, we have employed Interferometric scattering Microscopy (ISCAT) to explore the dynamics of a biotinylated lipid analogue labelled with streptavidin-coated gold nanoparticles (20 and 40nm in diameter) at 2kHz sampling rate. We developed a statistics-driven analysis pipeline to analyse both ensemble average and single trajectory Mean Squared Displacements from each dataset, and to discern the most likely diffusion mode. We found that the use of larger tags slows down the target motion without affecting the diffusion mode. Moreover, we determined from our statistical analysis that the prevalent diffusion mode of the tracked gold-labelled lipids is compartmentalized diffusion. This model describes the motion of particles diffusing on a corralled surface, with a certain probability of changing compartment. This is compatible with the picket-fence model of membrane structure, already observed by similar studies. Through our analysis, we could determine significant physical parameters, such as average compartment size, dynamic localization uncertainty, and the intra- and inter-compartmental diffusion rates. We then simulated diffusion in an environment compatible with the experimentally-derived parameters and model. The closeness of the results from the analysis of experimental and simulated trajectories validates our analysis and the proposed description of the cell membrane. Finally, we introduce the confinement strength metric to compare diffusivity measurements across techniques and experimental conditions, which we used to successfully compare the present results with other related studies.

Introduction

Cellular lipid membranes are an intensely researched object in modern Biophysics, due to their relevance to many fundamental cellular processes, such as cellular signalling [1], [2]. The lateral dynamics of their lipid component have proven particularly challenging to study. Given that the relevant spatiotemporal scales to probe range from the tens of nanometres to

the micrometre, and from microseconds to seconds, only few experimental techniques are able to approach the problem adequately [3]–[6]. Optical microscopy approaches have proven particularly successful in this regard and even more so since the achievement of super-resolution microscopy.

SPT is arguably one of the earliest quantitative approaches to optical microscopy, being used to probe molecular movements already more than a century ago [7]. Since then, the fields of application of SPT have only increased, together with the tools used for single-particle detection. Fluorescence-based SPT has the advantage of preserving the specificity characterizing fluorescence imaging. However, due to the long exposure times needed to achieve sufficient signal levels, conventional fluorescence microscopy has not achieved framerates faster than 2kHz [8], [9] with diffraction-limited detection. The recently developed MINFLUX, which has not yet been applied to membrane lipid tracking, has been reported to track molecules at kHz sampling rates, while simultaneously achieving nanometre-scale localization precision [10], [11]. At the state of the art, however, the fastest sampling rates (up to 50kHz) have been reported in scattering detection-based experiments, through the use of larger nanoparticle tags and advanced camera equipment [12]. These levels of temporal resolution, with claims of nanometre level of localization precision, have been initially performed using conventional brightfield microscopy, Differential Image Contrast, and variations thereof [13]–[17]. Other techniques, recent evolutions of Interference Reflection Microscopy [18], [19], Interferometric Scattering (ISCAT) and Coherent Brightfield (COBRI) Microscopy, also managed to approach such levels of temporal resolution in SPT on cell membranes in recent years [20]–[25].

The advantage held by ISCAT microscopy lies in how the final image is generated: the reflected and backscattered originated by the incident field generate an interference figure on the camera sensor [26]. In COBRI, the interference is instead generated by the transmitted field and the forward-scattered component of the incident light [27]. The imaging contrast is given by the phase difference term between the incident and reflected field, whereas the pure scattering component is, by comparison, negligible. This results in increased Signal to Noise (SNR) ratios compared to darkfield and brightfield microscopy, which instead rely exclusively on the light scattered by the tags [28]. This has allowed the use of smaller and smaller tags to probe particle motion, in the hope of reaching pure label-free detection [20], [29], [30]. Nevertheless, the continued use of gold nanoparticles carries the obvious advantage of unparalleled scattering capabilities, leading to high signal-to-noise ratios. Although the possibility of crosslinking is more than concrete [31], it has already be shown in a previous work that this would only slow down the diffusion and not alter the diffusion mode itself [32]. Given the relative simplicity of the experimental setup and the data analysis, these interferometric microscopy approaches have already been employed to perform SPT experiments on model and cellular membranes [21]–[23], [32]–[37].

The technical advances leading to faster framerates, however, also generate new problems in the analysis of SPT trajectories. The analysis of SPT data is largely reliant on the relation between the Mean Squared Displacement (MSD), the diffusion coefficient (D) and the time interval at which the displacements are calculated $n\ \delta t$, elaborated independently by Einstein

and von Smoluchowski [38]–[40]. Importantly, this relation does not account for inevitable experimental errors, such as a non-zero localization uncertainty, since it only takes into consideration the "real" positions of the diffusing particles. Therefore, the formulation has to be adapted to experimental data analysis. In fact, it has already been shown that particle detection in the context of non-zero localization uncertainty produces a positive offset to the MSD curve [41]–[43]. In addition to this linear effect, experimental data further suffers from motion blur, which naturally affects the detection of moving particles. This effect, which depends on experimental time resolution, generates a negative offset proportional to the time interval δt, thereby influencing especially the data at short time lags[44]. Moreover, if the sampling frequency of the experiments is too high compared to the diffusion rate, the diffusion behaviour of the targets can appear inhomogeneous, and slower, at short time scales [2], [45]. The main cause of these shortcomings is the underestimation of localization uncertainty. One of the most widespread method to assess this parameter is the variability in the relative distance between two immobilized tracers, as initially done in [46]. In the case of lower time resolution, when the distance covered by the tracked particle is much larger than the localization uncertainty, the effect is negligible [32]. Conversely, as the time resolution increases, the amount each particle moves between frames becomes comparable to the localization uncertainty, which then has a high potential for causing misleading conclusions [47]. More details on the topic of localization uncertainty estimation are given in the Materials and Methods section.

The aim of this work is to demonstrate the general applicability of ISCAT microscopy to accurately describe lipid dynamics on cellular membranes at frame rates of 2 kHz, with a very simple protocol and minimal materials required (Figure 1a). Since the interpretation of single molecule tracking studies on live cell membranes are typically very complex, due to the heterogeneity of motion modes [2], we hereby propose and validate an analysis pipeline for SPT trajectories which explicitly addresses this issues. The distinguishing features of the proposed analysis protocol are the estimation of the dynamic localization uncertainty and the implementation of a statistically robust, data-driven method of trajectory classification based on the identification of the most likely diffusion mode by statistical means. The main strength of this method is that it does not require *a priori* assumptions of which diffusive model is the most appropriate for a given trajectory, or an experiment altogether, but allows for a thorough evaluation of a set of diffusion modes, Thus, we provide a flexible and expandable strategy for the statistical determination of the most likely model for each data set and analysis time window. We show that the ensemble average diffusive motion of biotinylated phospholipid analogues labelled with streptavidin-coated 20nm or 40 nm diameter (Ø) gold nanoparticles on the plasma membrane of PtK2 cells is best described by a compartmentalized, or "hopping", diffusion model with a compartment size of ≈ 100 nm, although with different quantitative results as previously shown in comparable situations [13], [14]. Furthermore, we show that the ratio of single trajectories following the different diffusion modes are mostly independent from the size of the gold nanoparticles. Nevertheless, the diffusion coefficients of lipids tagged with Ø40 nm gold particles is lower than those of lipids tagged with the smaller Ø20 nm gold particles at all time scales. The observed difference stems solely from a 1.5 times lower inter-compartmental diffusion coefficient for the larger particles as compared

to the smaller particles. This reinforces the finding that the main effect of tag size is a diffusion slow-down, as expressed in a previous study [32]. We furthermore confirm the accuracy of our conclusion by comparing the results obtained through our data analysis pipeline to simulated trajectories of particle diffusion on a bidimensional lattice. By manipulating parameters such as the probability of the particle "hopping" between compartments, the diffusion coefficient and the localization uncertainty, we indeed validate that the motion of lipids on a cellular membrane is influenced by an underlying compartmentalization. This comparison to simulated trajectories furthermore suggests that the lipids tagged with the larger Ø40 nm gold nanoparticles have almost half the probability of "hopping" to the adjacent compartments, when compared to the lipids tagged with the smaller Ø20 nm gold nanoparticles. Finally, we define the ratio of the intra-compartmental and the inter-compartmental diffusion coefficient as a confinement strength metric that allows for a straight-forward comparison of the present results with other related studies from the same or other related techniques such as FCS and STED-FCS. The use of this metric shows that the diffusive motion herein described appears to not be cell line-specific, as demonstrated by comparison with the data from past experiments [47], [48].

Materials and Methods

Lipids and cell line

Atto488-labelled DOPE(1,2-Dioleoyl-*sn*-glycero-3-phosphoethanolamine) was purchased from Atto-Tec. DSPE-PEG(2000)-Biotin (DSPE: 1,2-distearoyl-sn-glycero-3-phosphoethanolamine, 2kDa PEG linker between the phospholipid polar head and the biotin), henceforth referred to simply as DSPE-PEG-Biotin, was purchased from Avanti Polar Lipids. Lipid stock solutions were stored at -20C in chloroform. Gold Nanoparticles of 20 nm and 40 nm diameter (Ø), streptavidin coated, where purchased from BBI solution in stocks, the concentration of which is expressed as 10 OD (optical density). PtK2 cells derived from rat kangaroo (Potorus tridactylis) kidney tissue [49] were available in the laboratory. These were cultured following known protocols, growing them in Dulbecco Modified Eagle Serum (DMEM, Sigma Aldrich), supplemented with ~15% FBS (Fetal Bovine Serum), L-Glutamine, and Penicillin-Streptomycin [50]. Before labelling and experiments, the cells were grown in sterile single-use flasks, placed in a 37C incubator in water vapour-saturated atmosphere with 5% CO2.

Cell membrane labelling

PtK2 cells were seeded and left to proliferate on methylated-spirits cleaned glass supports (25mm diameter, #1.5 thickness coverslips), and used at a stage where they did not yet reach confluency. A sufficient separation between the cells is deemed necessary to ensure that the membrane of each cell was not affected by the presence of neighbouring cells that may cause deformation. This translates to an estimated 50-70% confluency. Before the labelling, to allow a more comfortable and secure application of the labelling protocol, the glass supports were mounted in a water-tight steel chamber (Attofluor chambers, Thermo Scientific). The

cell labelling procedure was adapted from the protocol described in [51]. A stock solution of DSPE-PEG-Biotin in 1:1 Chloroform-Methanol at 10mg/ml was desiccated via nitrogen gas flow, and the lipid suspended again in absolute ethanol to a concentration of 20 mg/ml. This was diluted in L15 medium to a final concentration of 0.2mg/ml, and incubated at 37C for 20-30 minutes. In the same buffer, a small concentration of Atto488-DOPE was dissolved, in order to facilitate detection of the labelled cells by using the fluorescent channel of the ISCAT microscope. After the incubation with the biotinylated lipids, the cells were washed with fresh L15 buffer, and incubated for 10-15 minutes at 37C with a solution of 0.6uM of streptavidin-coated 20nm or 40 nm diameter (Ø) gold nanoparticles in L15 buffer. Afterwards, the cells were once again rinsed with fresh L15 buffer, and used for the experiments. This protocol produced a sparse labelling of cells (~1-2 nanoparticles per cell, with multiple labelled cells), good for single particle tracking.

Interferometric Scattering and Total Internal Reflection Microscope setup

ISCAT experiments were performed on a custom built, following the protocol in [52], that has been previously described [32] with some useful modifications. The output from a 650nm solid-state laser diode (OdicForce) was scanned in two directions (equivalent to the x and y on the sample plane) by two acousto-optic deflectors (AOD, Gooch & Housego and AA Opto-Electronics). The scanned output was then linearly polarized, relayed to the back focal plane of the objective via a two-lens telecentric system, passed through a polarizing beam splitter and circularly polarized by a quarter wave plate (B.Halle). The light was finally focused by a Plan Apochromatic 60x, 1.42NA oil immersion objective (Olympus), mounted in an inverted geometry. As stated in the introduction, the reflected component by the glass-sample interface and the back-scattered component by the sample were collected by the same objective, and reflected onto the detection path by a polarizing beam-splitter. The final image is obtained by focusing these two interfering beams onto the CMOS camera sensor (Photonfocus MV-D1024-160-CL-8) to acquire time lapses with an effective magnification of 333x (31.8nm effective pixel size).

In addition to this imaging mode, the microscope was also equipped with a total internal reflection fluorescence-capable channel. A 462nm wavelength solid state laser diode output was focused on the back aperture of the objective. TIR illumination condition was achieved via a movable mirror, until the reflection of the illumination beam was visible on the other side of the back-aperture. The fluorescence signal was separated from this reflection by means of an appropriately placed dichroic mirror, and imaged onto a difference CMOS camera (PointGrey Grasshopper 3). The labelling of cells with a fluorescent lipid analogue ensured that the sample could be correctly identified in a second, independent way. However, this part of the setup was not optimized to perform fluorescence imaging experiments, and it was used merely as a guide for the user.

Stabilization of the imaging plane was achieved by a piezo-actuated objective positioner (PiezoSystem Jena) in open-loop configuration. This ensured enough stability in the focus to perform the intended measurements. A summarizing scheme for the imaging setup is given in Supplementary Figure 1.

Imaging conditions

The glass support with the cells was positioned on the microscope stage while still inside the steel chamber used for labelling. The deformation in the support induced by the O-ring present in the steel chamber produced a drift in the apparent z position of the sample when changing area of imaging, but once readjusted, the sample was stable enough to allow prolonged observation times and correct recording, also thanks to the piezo-actuated objective positioner (MiPos, PiezoSystem Jena). The cells were imaged in L15 medium at a temperature of 37C, in room atmosphere and humidity, thanks to a temperature control dish (Warner Instruments). The laser power area density used to illuminate the cells for ISCAT imaging was 17.5 kW/cm2, and given the illumination wavelength used (660nm), temperature-induced artefacts can be ruled out [25]. Using the CMOS camera previously mentioned, we collected 2000 frames long movies in a 200x200 px^2 region of interest, equivalent to 2kHz sampling rate and roughly 41μm^2 imaging area. An evaluation of localization precision with these conditions has been derived by measuring the FWHM of the distribution of relative distances of two immobilized gold nanoparticles on glass, according to the procedure in [21], [46], [53], giving the value of 2.6nm.

Trajectory detection

Single Particle Tracking data analysis requires the trajectories of the particles to be extracted from the collected movies. The movies were collected in TDMS file format with a LabView software (courtesy of the Kukura Laboratory, University of Oxford), and converted to TIFF image stacks with a home-written MatLab code, based on the ConvertTDMS function by Brad Humphreys (https://www.github.com/humphreysb/ConvertTDMS, last retrieved March 23, 2020). Before particle tracking, all the movies were elaborated by subtracting the median filter, as previously elucidated [32]. In addition to this, the average intensity projection of the movie was obtained and subtracted from every movie frame, in order to separate the moving fraction of the sample from the static background (Supplementary Figure 2). Image analysis was performed using the FIJI platform [54]. Tracking was performed using the Spot Detection function in Imaris 9.5 (Bitplane, Oxford Instruments). Subsequent trajectories were imported in text format for post-processing in Mathematica (version 12.0.0.0; Wolfram Research) with custom written codes.

Analysis of Single Particle Trajectories

In order to thoroughly analyse and extract correct information from the collected data, we have refined the data analysis protocol that was previously introduced [2], [47]. The distinguishing features of this analysis protocol is the treatment of the localization uncertainty and the implementation of a robust, data-driven statistical method of single trajectory classification based on the most likely model of diffusive motion from a set thereof. Furthermore, in order to form a robust analysis pipeline with constant statistical sampling of measured displacements, we have restricted our analysis to single trajectories that contained at least 500 consecutive localizations, thus corresponding to a trajectory duration of 250 ms at

our sampling rate of 2kHz. Furthermore, we truncated all trajectories into segments of 500 consecutive localizations.

We calculated the Mean Squared Displacements (MSD), for each single trajectory from

$$MSD\ (t_n) = \frac{1}{N-n}\sum_{i=1}^{N-n}(r_{i+n} - r_i)^2 \qquad (Eq.1)$$

where r_i is the particle position at time t_i, for all available displacements at a given time lag interval t_n=n δt, where δt is the interval between two successive observations of the same particle, in this case 0.5ms, resulting from a sampling frequency, 1/ δt, of 2kHz. In the text, we refer to "single trajectory analysis" when the data arising from each single trajectory is analysed, and to "ensemble average" analysis when the MSD values of the trajectories belonging to the same dataset are averaged and then analysed.

The conventional data analysis strategy is to subsequently fit the experimentally determined MSD(t_n) dependence for a particular analysis time range, $t_{start} \leq t_n \leq t_{stop}$ to a relevant model of diffusive motion such as the expression Brownian (free) diffusion on a two dimensional plane, i.e.

$$\mathrm{MSD}(\mathrm{t}_n) = 4\ \mathrm{D}\ \mathrm{t}_n\ \left(1 - \frac{2\mathrm{R}}{\mathrm{n}}\right) +\ 2\ \delta_r{}^2 \qquad (Eq.2)$$

where we have also included two factors that are necessary for experimental MSD data. These correction factors are: 1) an additional correction factor, (1-2R/n), to account for motion blur as a consequence of particle motion during the camera integration time [44], and 2) a constant term, 2 δ_r^2, to account for the dynamic localization uncertainty by which each particle position can be determined. The motion blur correction term, which primarily affects the first few data points n, depends on the mode of illumination of the sample. In the case of full frame averaging, as employed here, R=1/6 [44]. The localization error term, 2 δ_r^2, which contributes a constant y-offset, primarily depends on the signal-to-noise of the microscope set-up where δ_r is the dynamic localization uncertainty $\delta_r^2 = \delta_x^2 + \delta_y^2$ or $\delta_r^2 = 2\ \delta_{x,y}^2$ if the localization uncertainty is symmetric in the x and y directions. These correction factors are an absolute requirement for fast sampling rates as these factors make the trajectories highly non-linear even when simple free diffusion is involved [44], [55].

While Eq. 2 is suitable for quantitative analysis, we find it much more informative, due of the complexities that are introduced by the above correction terms, to instead transform the MSD(t_n) data to the same units of [length^2/time] as the diffusion coefficient for our case of 2D diffusive motion on a plane as.

$$D_{app}(t_n) = \frac{MSD(t_n)}{4\ t_n\left(1 - \frac{2R}{n}\right)} \qquad (Eq.3)$$

The right-hand side of Eq. 3 can be thought of as an apparent diffusion coefficient, $D_{app}(t_n)$ from which it is now possible to directly evaluate the time dependence of the diffusive process from the trajectory data even in the absence of curve fitting to any specific model.

The data, transformed to the format of Eq. 3, was subsequently analysed by least squares non-linear curve fitting to a range of theoretical models for diffusive motion, all of which directly incorporated the camera blur corrected effect of localization noise as shown in Eq. 2. The generic relationship for the data models that we used for this analysis was

$$D_{app}(t_n) = D(t_n) + \frac{2{\delta_r}^2}{4t_n\left(1 - \frac{2R}{n}\right)} \qquad (Eq.4)$$

where we have split the calculated apparent diffusion coefficient $D_{app}(t_n)$ into its two distinct contributions: 1) the diffusive process $D(t_n)$, and 2) a camera blur-corrected localization error term, in which δ_r is the localization uncertainty.

The diffusion component $D(t_n)$ in Eq. 4 takes on different formulations to describe a range of theoretical diffusive motion models. In this work we have considered five models for the diffusion component, corresponding to immobile particles, simple Brownian (free) diffusion, confined diffusion, transiently confined (hop) diffusion, and directed motion, to be fitted to camera blur-corrected experimental data (as determined from Eq.3). The expressions for these models are [2]:

Immobile particles:

$$D(t_n) = 0 \qquad (Eq.5)$$

Brownian (free) diffusion:

$$D(t_n) = D_M \qquad (Eq.6)$$

Confined diffusion:

$$D(t_n) = D_\mu\left(\frac{\tau}{t_n}\right)\left[1 - exp\left(-\frac{t_n}{\tau}\right)\right] \qquad (Eq.7)$$

Compartmentalized (Hop) diffusion:

$$D(t_n) = D_M + D_\mu\left(\frac{\tau}{t_n}\right)\left[1 - exp\left(-\frac{t_n}{\tau}\right)\right] \qquad (Eq.8)$$

Directed motion:

$$D(t_n) = \frac{v^2 t_n}{4} \qquad (Eq.9)$$

We thus fit the models obtained by appropriately substituting Eq. 5-9 in Eq. 4 to the $D_{app}(t_n)$ values obtained through Eq. 3. The least-squares fitting routine was implemented in Mathematica (version 12.0.0.0; Wolfram Research) using the NonlinearModelFit[] command

with a Confidence Level of 0.99. While devising our analysis method, we have further explored the effect of the data weighing strategy on the non-linear fits (data not shown). The conventional data analysis strategy for single particle tracking data prescribes that the MSD data at each time point t_n should be fitted to a pre-determined motion model with weights equal to the inverse variance of each point. As a consequence of this, greater emphasis is given to the short time lags, as emerges from the plot of relative fit weights versus time lag t_n. However, we found that the fit results are largely invariant whether the data are weighed according to the inverse variance, to the variance or unweighted, with minor deviations observable only in the magnitudes of the standard errors (s.e.) associated to the fit parameters. This invariance indicates that our data analysis routine is indeed very robust. We have therefore opted to perform unweighted fits in this study, as this strategy places the same emphasis on all time points [55].

Note that the compartmentalized diffusion model (Eq. 8) can be thought of as the sum of time-independent Brownian diffusion (Eq. 6) and time-dependent confined diffusion (Eq. 7). Specifically, the observed intra-compartmental diffusion coefficient within the confining compartment (i.e., the limit of t=0) is the sum of the two components, $D_0 = D_M + D_\mu$ while in the limit of $t \gg \tau$, the inter-compartmental diffusion coefficient is D_M. The free diffusion model (Eq. 6) thus represents the case where a molecule diffuses freely between compartments (i.e. $D_\mu=0$), while the confined diffusion model (Eq.7) represents the case where the molecule never leaves the confinement zone (i.e. $D_M=0$). The compartmentalized diffusion model thus represents mathematically the possibility of the particle to transition from one compartment to the other. We can derive another quantity from the confined and compartmentalized diffusion models, that is, the average compartment size, L [56]:

$$L = \sqrt{12 D_\mu \tau} \qquad (Eq. 10)$$

and the average compartment confinement time, τ_{Conf}

$$\tau_{Conf} = \frac{L^2}{4\, D_M} \qquad (Eq. 11)$$

In this analysis, we have further directly included the dynamic localization uncertainty, δ_r, as a free parameter in the least square fit. This is a different approach to already explored methods, where this quantity is either not taken into account during the derivation of parameters relevant to describe the diffusive motion of the particles, or just used as a baseline value to subtract to the entire dataset [57]. Another issue is represented by the estimation of the localization error. In other cases the localization error is estimated by measuring the degree of variability in the relative distance of two immobilized tags [46]. In the case of ISCAT microscopy, the majority of studies (e.g. [21], [58]) report the localization uncertainty of the setup as the average of the standard deviations of repeated localization of immobilized particles (or molecules), determined by fitting the intensity profiles of detected particles to a 2D spatial Gaussian. We offer the value derived in this method these metrics in Supplementary Figure 3 and Supplementary Table 1.

Statistical evaluation of the most likely diffusion model

In this work, we have chosen to apply a data-driven analysis pipeline that does neither require *a priori* knowledge nor assumption of the relevant diffusive motion model for a particular data set. This approach is a refined extension to our previous work [47] with new modifications that were aimed at increasing the robustness of the approach in order to extend the applicability to the analysis of single trajectories. The challenge of analysing single trajectory data in this context stems from the fact that single trajectories are in general much noisier than the equivalent ensemble average of each dataset trajectories as the averaging step involves significantly fewer displacements.

In this modified approach, we determined as previously the most likely diffusion model, from a set of plausible models (Eqs.5-9), by calculating the Bayesian Information Criterion (BIC) from the results for each data model, according to the formula [59]:

$$BIC(model) = n \ln\left({}^{RSS}/_{n}\right) + k \ln(n) \qquad (Eq.\,11)$$

where n is the number of data points used for the fitting, RSS is the residual sum of squares, and k is the number of free parameters in the fit. The first term in Eq. 11 is a measure of the Goodness of Fit while the second term adds a penalty function that increases linearly with the addition of each free parameter to the model. In general, a smaller BIC value equates to better fit quality. Using the calculated BIC values for each model we can then calculate the relative likelihood of each model by using the formula:

$$Relative\ Likelihood = Exp\left[\frac{BIC(model)_{Min} - BIC(model)}{2}\right] \qquad \text{(Eq. 12)}$$

where $BIC(model)_{Min}$ is the lowest BIC value from the model fits. Therefore, the model with the smallest BIC value thus has a Relative Likelihood of 1 while all other models have Relative Likelihood <1.

To enhance the robustness of this approach, we have here further introduced a second requirement to ensure that all free parameters in a given model fit converged to a non-zero magnitude at a significance level of $p<0.05$. The t-statistics are determined as the fit parameter estimates divided by the standard errors, and the p-values are the two-sided p-values for the t-statistic, with the null hypothesis being that the parameter is equal to zero. Using these two metrics, the best model to describe each trajectory therefore has to satisfy two conditions: having the smallest BIC (i.e., the highest Relative Likelihood) of all models, and that the fit parameters pass the aforementioned t-test. If the most likely fit does not satisfy the second condition, the model with the second-smallest BIC, but which satisfies the t-test condition is then selected, and so on. Finally, if no model is able to simultaneously satisfy both conditions, then that data is excluded from further analysis. Additionally, in the case of single trajectory analysis, which naturally suffers from greater noise than the ensemble average of all the curves, we also require that the coefficient of variation (R^2) for each diffusion model had to be $R^2>0.9$ for the trajectory to be included in the analysis. This modified data analysis approach establishes a robust unbiased statistical methodology for

determining the most likely type of diffusive motion model, from a particular given set of evaluated motion models, however our approach cannot provide judgement on non-tested models.

Sampling of data points in analysis pipelines

One of the challenges in the analysis of SPT data is that there is currently no consensus with regards to the amount of data points which should be analysed in order to describe the nature of the diffusion motion of the tracked particle [60]. Therefore, we have performed curve fitting across six different time intervals defined as 0.5 ms ≤ t_n≤ T, with T equal to 5ms, 10ms, 25ms, 50ms, 75ms, and 100ms. For T=5ms and 10ms, all the values of $D_{app}(t_n)$ (10 and 20, respectively) were used in the fitting operation. In the remaining cases, we have instead sampled the data on a temporal logarithmic scale. In this case, we first converted the time values to a natural logarithmic scale, and resampled the time points at fixed intervals of width $(\log_{10} T - \log_{10} t_0)/(0.5 * T/t_0)$. For example, for T=50ms (corresponding to n=100 data points), we selected time points that were spaced (Log[50ms]-Log[0.5ms])/75 apart. After rounding to the closest values and removal of duplicate time points, this resulted in 46 roughly evenly spaced time points on a log scale where n={1, 2, 3, 4, 5, 6, 7, 8, 9, 10, 11, 12, 13, 14, 15, 16, 17, 18, 19, 20, 22, 23, 24, 26, 28, 29, 31, 33, 35, 37, 40, 42, 45, 48, 51, 54, 58, 61, 65, 69, 74, 78, 83, 88, 94, 100} that we used for the fitting. This effectively serves to place extra emphasis on the initial time points where we observed the greatest change in magnitude of the apparent diffusion coefficient both due to the influence of the localization error and also due to transient confinement in compartments with a size range of about 100-500nm as was observed in the single trajectory fits.

Monte Carlo simulations of 2D diffusion in a heterogenous lattice.

Monte Carlo simulations were performed using custom written routines in Matlab as previously described [48]. In brief, in these simulations, we generated fluorescence time traces of 2-dimensional diffusion of single molecules in a heterogenous lattice. The simulation area was a square with side lengths of 8 to20 μm (the dimensions of the area are not influential) and the compartmentalisation of this area was implemented as a Voronoi mesh on a uniform random distribution of seed points. We defined the square root of the average compartment area as the average compartment size or length L. The average compartment size (L), defined as the square root of the average compartment area, the hopping probability (P_{hop}) and the free diffusion coefficient (D_S) completely described our simulation model. Within a compartment the molecules were assumed to diffuse freely while crossing from one compartment to another is regulated by a "hopping probability" P_{Hop}. This was implemented in the following way: if the diffusion motion (with diffusion coefficient D_S) would make the lipid to cross the compartment boundary, a random number is generated, and the movement takes place only if this number is above the threshold defined by P_{Hop}. In all other cases, a new displacement is calculated, where the molecule would be diffusing in the same compartment. In the special case of free Brownian diffusion (i.e. P_{Hop}=1) each collision with a compartment boundary results in a molecule crossing to the adjacent compartment. When P_{Hop}<1, e.g. for P_{Hop}=1/40, only 1 out of 40 collisions with a compartment boundary

results in a molecule crossing to the adjacent compartment. For each condition (D_S, L_S, and P_{hop}), we simulated N=100 trajectories with 0.5 ms time steps (i.e. a sampling rate of 2 kHz) and a time span of 250 ms (i.e. 500 displacements per trajectory). Subsequently, we added simulated localization noise to each trajectory centroid position $\{x_i,y_i\}$ by addition of a random noise factor $\{\Delta x_i,\Delta y_i\}$ of $\{\pm \delta_{x,} \pm \delta_y\}$ where $\delta_x=\delta_y= \delta_{x,y}$ and $\delta_r^2=2\ \delta_{x,y}^2$. These trajectories were subsequently analysed by use of same data analysis pipeline as for the experimental ISCAT data except that the camera blur correction factor was R=0.

Results and Discussion

Labelling and imaging of cells

In this work, we have used ISCAT microscopy to investigate the lateral diffusion in the plasma membrane of live PtK2 cells of artificially incorporated biotinylated phospholipids, DSPE-PEG2000-Biotin, tagged with either Ø20 nm or Ø40 nm streptavidin-coated gold nanoparticles. In order to avoid false detections, whereby a moving particle could be detected, for example, diffusing outside of a cell, the cell membranes were also labelled with a fluorescent lipid (Atto488-DOPE), and simultaneously imaged using the TIRF channel present in our setup (see Materials and Methods). The movies of diffusing particles where then recorded only in the areas where a fluorescent signal corresponding to a cell was detected.

ISCAT microscopy enables the collection of long, continuous single particle trajectories at 2 kHz frame rates

The main challenge in the data analysis of diffusing particles is the stochastic nature of this phenomenon. Consequently, the robustness in the determination of descriptive physical parameters of any such process by SPT is significantly improved by the availability of long, preferably continuous single particle trajectories. Furthermore, the sampling frequency of the data acquisition needs to be sufficiently rapid to resolve permanent or transient confinements into compartments in the tens to hundreds nanometres range [13], [14], [61]. Using our ISCAT set-up, we have been able to acquire long, continuous, trajectories of diffusing biotinylated lipid analogues (DSPE-PEG(2000)-Biotin), inserted in the plasma membrane of live PtK2 cells, and labelled with either Ø20nm or Ø40nm streptavidin-coated gold particles at a sampling frequency of 2 kHz. The statistics for the acquired and subsequently analysed experimental data of nanoparticle-tagged lipids on PTk2 cells and for gold particles immobilized on a glass substrate are summarized in Table 1. The superimposed ensembles of the track segments are shown in Fig. 2a for Ø20nm and Fig. 2d for Ø40nm gold particles. Although this visualization cannot give detailed information on the diffusion mode, or physical quantities thereof, it is still apparent that the gold particle-labelled DSPE lipids on PtK2 cells diffuse from the centre in a broadly symmetrical manner, reflecting the stochastic nature of the long-term motion of the tracked particles.

Implementation of a robust data driven approach for quantitative analysis of single particle trajectories

In this work, we have implemented a data-driven method to determine the most appropriate model to describe the diffusive motion of the gold nanoparticle-tagged lipids detected. This method, which is suitable for both the ensemble average analysis and single trajectory analysis, requires neither *a priori* knowledge, nor assumptions of the physical characteristics of the underlying environment. In this approach, which extends our previous work [47], we first performed least-squares non-linear curve fittings of a set of plausible models (Eq. 5-9) to the apparent diffusion coefficient $D_{app}(t_n)$ (Eq. 4) curves derived directly from the experimental tracking data. For increased robustness, our pipeline further incorporates two goodness of fit criteria: 1) that all free parameters in a given model are significantly non-zero, and 2) that the coefficient of variation (R^2) for the specific diffusive model respected $R^2>0.9$. These criteria are especially important for enhancing the robustness of the fitting pipeline in the case of single trajectories. This is because single trajectories are more subject to noise sources (e.g., environmental vibrations) than the corresponding ensemble averages as a consequence of the much lower data sampling at each $D_{app}(t_n)$ data point. To further improve the convergence of the model fits to the single particle trajectories (by limiting the number of free parameters in these fits), we fixed the value for the localization uncertainty δ_r to the one obtained determined from the analysis of the corresponding ensemble averaged data, for each time regime. The evaluation of which model is most suitable to describe the diffusive motion of the tracked particle is performed through purely statistical means (see Materials and Methods). A representative example of the output results for this analysis routine is shown is shown in Supplementary Figure 4, while the resulting fit quality metrics are listed in Supplementary Table 2. In this example, the ensemble average D_{app} data for Ø20nm gold particles-tagged lipids on a PtK2 cell membrane, the most likely model turns out to be compartmentalized diffusion (Eq. 8). All other models are rejected purely on the basis of fit quality, and ranking by relative likelihood. This analysis routine thereby provides a readily expandable and fully automatable strategy for the statistical determination of the most likely diffusion model for a specific data set. In addition to this, we would like to stress how the adoption of the apparent diffusion coefficient, and consequently of the related diffusion models (Eq. 5-9), gives us direct access to a direct method to probe the physical characteristics of the environment on which the target particles diffuse, such as compartment length in the case of compartmentalized or confined diffusion (Eq.10).

The quantitative ensemble average analysis results are largely invariant for analysis time regimes $0.5\text{ms} \leq t_n \leq T$ *with* $10\text{ ms} \leq T \leq 100\text{ ms}$

We applied the data analysis routine to our ISCAT tracking data of Ø20 nm and Ø40 nm streptavidin-coated gold particle-tagged DSPE-PEG2000-biotin lipids on PtK2 cell membranes, and to the same gold particles immobilized on a glass surface. One of the challenges in the analysis of SPT data is that there is no consensus regarding the amount of points of a MSD curve to be analysed in order to properly describe the diffusion motion of the tracked particle [60]. For this reason, we evaluated the dependence on the fit results upon the analysis time range for six different time intervals, $0.5\text{ms} \leq t_n \leq T$, where T was set to 5ms,

10ms, 25ms, 50ms, 75ms, or 100ms. At the employed sampling frequency of 2kHz, this corresponds to 10 (2%), 20 (4%), 50 (10%), 100 (20%), 150 (30%), and 200 (40%) points of the 500 localization long segments extracted from the full-length trajectories.

From our analysis, we found out that the most likely model to describe the time-dependence of the ensemble averages $D_{app}(t_n)$ curves for both the Ø20 nm and Ø40 nm gold particle-tagged lipids is consistently the compartmentalized (Eq. 8) diffusion model (Figure 3a, b). This is true for most analysis time ranges, apart from the smallest time window ($0.5 \leq t_n \leq 5$ms), whereby the average data for Ø20 and Ø40 nm gold particle-tagged lipids on PtK2 cells is instead best described by the confined diffusion model (Eq. 7). The values for the ensemble average fit parameters for each analysis time window are plotted in Figure 4a-f. The corresponding parameter estimates for the ensemble average $D_{app}(t_n)$ data are shown in Supplementary Tables 3 (Ø20 nm gold particle-tagged lipids) and 4 (Ø40 nm gold particle-tagged lipids). These plots show that the fit parameters converge to fairly consistent values at time windows larger than 5ms. This suggests that the shortest time window is not sufficiently long to accurately differentiate between confined (i.e., an inter-compartmental diffusion rate of D_M=0) and compartmentalized diffusion (i.e., an inter-compartmental diffusion rate, D_M, ≥0). For these reasons, we find it necessary to adopt a time window for observation longer than 5ms. On the other hand, the slight divergence of the values for the average compartment size L and confinement time τ for longer than 50ms time windows, lead us to prefer an intermediate time window. We thus conclude that the analysis time range $0.5\text{ms} \leq t_n \leq 50\text{ms}$ is the optimal range for the $D_{app}(t_n)$ data analysis for experimental data such as ours, where we observe compartmentalized diffusion with a compartment size around 100 nm. Given that our detected tracks are cropped to equal segments of 500 localizations, corresponding to 250 ms at our 2kHz sampling rate, this means that 20% of the total data points are considered for analysis. This appears as a good compromise between the "rule of thumb", prescribing that no more than 25% of the total duration of the trajectories should be used for data analysis [60], [62], and using only the first few points, as recommended by Kusumi and co-workers [63], [64].

The magnitude of the ensemble average diffusive motion parameters, but not the motion type, are dependent on the probe characteristics

The fit parameters extracted from the analysis of the ensemble average $D_{app}(t_n)$ data provide a large wealth of information, both on the diffusive motion of the tracked lipids, and the plasma membrane on which they diffuse (Supplementary Tables 3 and 4). First of all, regardless of the size of the gold nanoparticle used to tag the biotinylated DSPE lipids, the most likely diffusion mode is the compartmentalized diffusion model (Eq. 8; fit results in Supplementary Tables 3 and 4). This diffusion mode enables us to distinguish between a long-range, time-invariant diffusive component D_M, and a short-range, time decaying diffusive component D_μ (Eq. 8). Our results for the fit parameters interestingly show that the sole effect of the gold nanoparticle size is that the long-range, time-invariant, diffusive component D_M is about 1.5 times larger for the lipids tagged with the Ø20 nm gold nanoparticles. At the recommended analysis time range of $0.5\text{ms} \leq t_n \leq 50\text{ms}$ this corresponds to a magnitude of $D_{M,\,Ø20} = 0.37 \pm 0.00\ \mu m^2/s$ for the smaller tags, compared to $D_{M,\,Ø40}$ =

0.24 ± 0.00 $\mu m^2/s$ for the larger ones. In contrast, we observe a substantial invariance across gold nanoparticle size of the average time-decaying diffusive components D_μ ($D_{\mu, Ø40}$ = 0.40 ± 0.02 $\mu m^2/s$ versus $D_{\mu, Ø20}$ = 0.41 ± 0.02 $\mu m^2/s$), and the average decay times τ ($\tau_{Ø40}$=2.0 ± 0.1 ms versus $\tau_{Ø20}$=2.1 ± 0.2 ms). This has the consequence that the average compartment sizes L, calculated from Eq. 10, were also very similar for both tags ($L_{Ø40}$ = 98 ± 3.8 nm versus $L_{Ø20}$ = 100 ± 5.0 nm), while the average confinement times τ_{Conf}, calculated from Eq. 11, were about 1.5 times greater for the larger nanoparticles than for the smaller ones ($\tau_{Conf\ Ø40}$=10±0.4 ms versus $\tau_{Conf\ Ø20}$=6.3±0.3 ms). The overall rate of diffusion, which is given by Eq. 8 for compartmentalized diffusion, is thus faster, at all time-scales, for lipids tagged with the smaller Ø20nm gold nanoparticles than for those tagged with Ø40nm gold nanoparticles.

In order to facilitate the interpretation of the diffusion motion thus detected, we define the intra-compartmental diffusion rate D_0 as the limit of D(t) for $t \to 0$, and the inter-compartmental diffusion rate D_∞ as the limit of D(t) for $t \to \infty$. For the compartmentalized diffusion model (Eq. 8) this equates to $D_0 = D_M + D_\mu$ and $D_\infty = D_M$, respectively. In the present experiments, both these quantities are, expectedly, markedly lower for the lipids tagged with the Ø40nm gold nanoparticles ($D_{0\ Ø40}$= 0.63±0.02 $\mu m^2/s$ and $D_{\infty\ Ø40}$= 0.24 ± 0.00 $\mu m^2/s$) compared to the ones tagged with Ø20nm gold nanoparticles ($D_{0\ Ø20}$= 0.77±0.02 $\mu m^2/s$ and $D_{\infty\ Ø20}$= 0.37 ± 0.00 $\mu m^2/s$). These results suggest that while the size of the probe certainly has a significant influence on the diffusion rate, likely due to a combination of its size and cross-linking potential, we have achieved a minimal labelling that does neither affect the diffusion mode nor the compartment size of the plasma membrane as derived from the model fitting routine. This conclusion is consistent with our previous findings [32], which show a similar effect in model membranes (i.e. Supported Lipid Bilayers) and live cells [47], [48], [65].

Finally, we draw attention to the dynamic localization uncertainty δ_r obtained for the gold nanoparticle-tagged diffusing biotinylated lipid analogues. The values obtained ($\delta_{r, Ø20nm}$=20±0.3 nm and $\delta_{r, Ø40nm}$ = 17±0.3 nm) differ substantially from those reported for similar setups and experimental conditions. However, we emphasize that the values hereby reported are directly obtained through our analysis pipeline of the $D_{app}(t_n)$ data derived from the trajectories of tracked lipids. As such, the localization uncertainty is determined at the same signal-to-noise ratio as the data themselves. The fact that the Ø40nm gold nanoparticles have a smaller localization uncertainty than the Ø20nm ones is a reasonable expectation, due to the larger scattering cross-section (i.e., larger signal-to-noise ratio) making the former easier to locate and track. The measure of how strongly the localization error affects the detected curves is evident from a comparison of the raw $D_{app}(t_n)$ data in Figure 3a and the localization uncertainty corrected $D(t_n)$ data in Figure 3b. The first few points are the ones where this operation has a more visible effect, since the localization uncertainty mostly affects short time lags. Moreover, after observing that the localization uncertainty is independent of the analysis time window (Supplementary Tables 3-6), we can conclude that our analysis pipeline is able to effectively estimate its value, without affecting the rest of the parameters. The increase in localization uncertainty is further validated by the fact that immobilized gold nanoparticle "tracks" are characterized by localization uncertainties

significantly lower than the ones used to label and track lipids on the plasma membrane (Supplementary Table 1).

The single trajectory analysis reveals the full complexity and heterogeneity of the lipid motion on the plasma membrane of Ptk2 cells

One of the advantages of SPT experiments lies in the possibility for revealing information about the extent of heterogeneity in the observed diffusive motion amongst single molecules. Such analysis does however require the availability of sufficiently long trajectories in order to enable a robust statistical sampling of displacements to ensure accurate analysis results [66]. While the availability of long, single molecule tracks is usually precluded due to photobleaching when using fluorescent dyes or proteins, this is not the case for scattering-based detection, as is the case here. Thus, we also applied our analysis pipeline to separately analyse each experimental single molecule track.

The results from the single trajectory analysis confirmed the notion that diffusive motion in the plasma membrane is complex and heterogeneous. These results are summarized in Figure 5 while the complete results of the fit parameter values are given in Supplementary Tables 7 and 9. Our analysis showed that the relative fractions of the most likely lateral motion model of the single trajectories, for both species of nanoparticles, were roughly constant in the time analysis ranges of $0.5\text{ms} \leq t_n \leq T$ for $10 \leq T \leq 100$ ms (Fig. 5a). In these time regimes, we found that a majority of the single trajectories were best described by the compartmentalized diffusion model (~50-60% for the larger Ø40 nm gold particles versus ~40-50% for the smaller Ø20 nm gold particles) but that there was also a significant fraction of trajectories that were better described as either free or confined diffusion. Specifically, the proportion of trajectories best described by the free diffusion model was slightly greater for the smaller Ø20 nm gold particles (~20% for $10 \leq T \leq 100$ ms) than for the larger Ø40 nm gold particles (~15-20% across the range of T). In contrast, the relative fraction of trajectories best described by the confined diffusion model were about the same (~10-20% with a slight variation depending on T) for both probe sizes. In contrast, the same analysis performed on a restricted analysis time range in the shortest time window ($0.5\text{ms} \leq t_n \leq 5\text{ms}$) shows that the lateral motion of most tagged lipids, for both probe sizes, is best described by the confined diffusion model. This last result, which is fully consistent with the ensemble average analysis, is caused by the fact that short analysis time intervals are not sufficient to fully capture the transition from intra-compartmental diffusion to inter-compartmental diffusion. From the largely invariant fit results in the analysis time ranges with $10\text{ ms} \leq T \leq 100\text{ms}$ (Fig 5a), we conclude again that a suitable time range for analysing SPT data that contains an apparent transition from microscopic to macroscopic diffusion due to compartment sizes in the 100-250 nm size range is to use a time analysis range of $0.5\text{ms} \leq t_n \leq 50\text{ms}$. We further note that the fact that the relative proportions of observed motion types are very similar for both probe molecules again suggests that the type of diffusive motion is only weakly dependent on the probe characteristics.

To further explore the observed diffusive motion heterogeneity, we applied the trajectory classification results to explore whether the ensemble average of each sub-

population of diffusive motion were distinct. A visual inspection of the superimposed trajectories classified according to motion type appears at best to show a tendency for greater displacement of trajectories away from the origin amongst the trajectories classified as free diffusion as compared to the other motion models (Supplementary Figures 6a and b). The full extent of the heterogeneity between the different motion modes is however most apparent from the broad distributions of each individual fit parameter for each classified motion mode from the single trajectory fits (Figures 5c-h. and Supplementary Tables 7 and 9). A closer inspection of these fit parameters by using a Mann-Whitney test (Supplementary Tables 8 and 10) revealed that the median values of most fit parameters were significantly different between the different lateral motion models. Furthermore, a comparison of the fit parameters for lipids diffusing with the same motion modes, but tagged with gold nanoparticles of different size showed that most parameters were significantly different (Supplementary Table 11). These results collectively validate that the lateral motion of phospholipids in the plasma membrane is very complex and further that the observed motion is partly dependent on the characteristics of the tag itself.

Interestingly a comparison of the resulting fit parameters for the compartment sizes L between the trajectories best described as confined diffusion respectively compartmentalized diffusion for an analysis time range of 0.5 ms $\leq t_n \leq$ 50 ms further suggested that there may be two distinct levels of compartment sizes in the plasma membrane of live cells. The first level of compartment sizes was characterized by transiently confined diffusion (i.e. D_M>0 $\mu m^2/s$) with a mean (±standard deviation) compartment size of $L_{Compartmentalized}$=140±55 nm (Ø20 nm gold nanoparticles) respectively $L_{Compartmentalized}$=120±45 nm (Ø40 nm gold nanoparticles). The second level of compartment sizes was characterized by permanently confined diffusion (i.e. D_M=0 $\mu m^2/s$) with a mean (±standard deviation) compartment size that was about 4 times greater (i.e. $L_{Confined}$=520±250 nm for Ø20 nm gold nanoparticles and $L_{Confined}$=430±270 nm for Ø40 nm gold nanoparticles). These results hint at the possible presence of a much greater heterogeneity in the diffusive motion in the plasma membrane than could be seen with our ensemble average analysis approach which in contrast revealed only a single level of compartments with a slightly smaller size ($L_{Ø20}$=100±4.6 nm, respectively $_{Ø40}$=98±3.5 nm). The revelation of the greater complexity by the single trajectory analysis approach is thus indicative of the possible presence of a much more complicated heterogeneous underlying plasma membrane structure than can be resolved by the ensemble average analysis.

Validation of data analysis by comparison to simulated trajectories for diffusion in a heterogenous lattice

In order to validate our data analysis approach and our observation, we next compared the results from our experiments to simulated trajectories on a compartmentalized surface as previously described (see Materials and Methods) [48]. This procedure enabled us to directly compare our observations with our hypothesis for the mechanisms generating the heterogeneities of diffusion on the plasma membrane, namely its compartmentalization. The necessary parameters to initiate the simulations are the probability of the particle to change compartment P_{Hop}, the diffusion coefficient D_S, the average compartment size L_S, and the

localization uncertainty $\delta_{r\,S}$. First of all, we noticed that the experimental ensemble average ISCAT data for Ø20 nm gold particles could be well approximated by simulated data with the following parameters: P_{Hop}=1/20, D_S=1.2 μm^2/s, L_S=120 nm, and $\delta_{r\,S}$=16 nm, while the data for Ø40 nm gold particles could be very well approximated by simulations with parameters P_{Hop}=3/100, D_S=1.0 μm^2/s, L_S=120 nm, and $\delta_{r\,S}$=12 nm (Figure 3c, Figure 4 and Supplementary Figure 7). Furthermore, we verified, through comparison between the input parameters and the results of the analysis routines of the simulated data, that our approach is able to adequately describe the simulated data and to extract meaningful physical parameters (Supplementary Text 1, Supplementary Figures 8, and 10-12, and Supplementary Tables 12 and 14-15).

This comparison shows that the accuracy of our analysis pipeline in analysing simulated date, however, is extremely sensitive to variation in the P_{Hop} parameter. In particular, we noticed that for the lowest values of P_{Hop}, the localization uncertainty tends to be overestimated (Supplementary Figure 8i and Supplementary Table 12). On the other hand, when P_{Hop} is higher, that is, in the case of weak compartmentalization, it is more challenging to distinguish between free and compartmentalized diffusion. Finally, the compartmentalization induced in the simulated surface leads to the underestimation of the diffusion coefficient, due to the reduced mobility of the particle caused by the compartment barriers. In the compartmentalized diffusion model (Eq. 8), this translates to a significant underestimation of D_μ, leading to a value for the intra-compartmental diffusion coefficient $D_0(=D_\mu+D_M)$ which differs significantly from the corresponding simulated diffusion coefficient D_S. This effect was noticeable for lower values of P_{Hop} (Supplementary Figure 8d), for increasing unhindered diffusion coefficients D_S (Supplementary Figure 10k), or decreasing compartment sizes L_S (Supplementary Figure 11k). This also results, due to the relationship between D_μ and L (Eq. 10) in the underestimation of the compartment size L compared to the simulated value L_S for low P_{Hop} values (Supplementary Figure 8h) and for decreasing simulated compartment sizes L_S (Supplementary Figure 11o).

These simulated trajectories further enabled us to confirm that our analysis pipeline can also be used with high accuracy for equivalent analysis at the single trajectory basis (Figure 5). In fact the best accuracy of the analysis pipelines, judged by comparing the fitted parameters with the simulated parameters, was achieved by the single trajectory analysis. In particular, the best description was achieved for the subset of trajectories best described as compartmentalized diffusion, when L≤120 nm and P_{Hop}≤1/10, a parameter range that is in line with our experimental data analysis values. Yet, a side-by-side comparison of the single trajectory analysis parameters for the experimental data and the simulated data with simulation parameters that closely resembled the ensemble average experimental data (Figure 3c) is, however, strongly suggestive of a much greater diversity in the structural organization of the cellular plasma membrane than can be approximated by simulations (Figure 5). In particular, the proportion of trajectories classified as free diffusion is much greater for the experimental data than for the matching simulated data (Figures 5a-b and Supplementary Figure 6) while the width of the distributions of all fit parameters is significantly greater for all detected motion modes (Figure 5). This again demonstrates the greater value of the single

trajectory analysis as opposed to the ensemble average analysis approach. We further note that the single trajectory analysis of simulated trajectories. as was the case for the experimental data analysis, consistently reveals a second layer of compartmentalization with about a 4x greater compartment size, albeit for a much smaller fraction of single trajectories than for the equivalent experimental data. However, the associated times τ are in the same range as the time regimes used for the fitting routines (Figure 5f). Thereby, it is very difficult to prove the existence of these larger compartments in the experimental data, as the simulations results show that this layer can also occur by chance.

The definition of a new metric, the confinement strength, which enables direct comparison of diffusion data obtained by various methods

In order to better represent the connection between our simulated data and the experimental data not only from this work, but also from related studies of lipid diffusion in related literature [47], [48], [65], it is useful to define a new metric, which we named confinement strength, S_{conf}. We define this value in relation to environments where a compartmentalized diffusion behaviour is plausible and detected, as the ratio between the intra-compartmental diffusion coefficient and the inter-compartmental diffusion coefficient. Following this definition, in the case of the compartmentalized trajectories detected in our experiments, and those we derive from the simulations, the extrapolated intra-compartmental diffusion is $D_0=D_\mu+ D_M$, whereas the extrapolated inter-compartmental diffusion coefficient at infinite time, $D_\infty=D_M$, and we calculate $S_{conf}= D_0/ D_\infty$. This parameter is strongly connected to the simulated P_{Hop} (Supplementary Figure 13a), but it is much less dependent on the other simulation parameters such as the diffusion coefficient D_S (Supplementary Figure 13b), the compartment strength L (Supplementary Figure 13c), and the localization uncertainty $\delta_{r\,S}$ (Supplementary Figure 13d). Thereby, it should provide with a representative descriptor of the physical landscape where the tracked particles are diffusing. By calculating this metric for the ensemble average data presented in this work, we obtain the values $S_{conf}=2.1\pm 0.1$ for the lipids tagged with the Ø20 nm gold nanoparticles, and $S_{conf}=2.6 \pm 0.1$ for the lipids tagged with the Ø40 nm gold nanoparticles (Table 2). From these results, we can confirm our observation that the larger probe size has a stronger influence on the detected motion of the target particle, resulting in a higher measured confinement strength. Nevertheless, when we compare these values with the S_{conf} obtained from the analysis of the ensemble average $D_{App}(t_n)$ data from the matching simulated trajectories (Table 2), we find a close resemblance with the corresponding values obtained from the experimental data.

In the broader context of comparison of the present data with relevant literature, the S_{conf} parameter also shows its potential for matching simulations of compartmentalized diffusion and experimental data extracted from relevant literature, and thus allows comparison between different methods to detect diffusion dynamics, such as Fluorescence Correlation Spectroscopy (FCS), and its combination with super-resolution STED microscopy (STED-FCS). For the experiments reported in [48], [65], where diffusion is detected via STED-FCS, the equivalent D_0 is taken as the diffusion coefficient detected via STED-FCS with the smallest detection spot (i.e., with the highest depletion laser power), whereas the D_∞ would be the one detected using the conventional diffraction limited spot. For

the experiment in [47], the D_∞ is the diffusion coefficient detected via FCS in the presence of CK666, which inhibits Arp2/3 mediated actin crosslinking, and thus the compartmentalization of the plasma membrane, whereas the D_0 is the same parameter measured in its absence. In Figure 6, we plotted the values for S_{conf} obtained from the experiment thus far presented and from the aforementioned related studies against the values of P_{Hop} estimated by matching simulations. To these points, we overlaid the values of S_{conf} and the corresponding P_{Hop} values derived from the ensemble average analysis of simulated trajectories with different values of P_{Hop} and other simulation parameters fixed at $D_S=1.0$ $\mu m^2/s$, $L_S=120$ *nm, and* $\delta_{r\,S}=20$ *nm*. Corresponding relevant parameters are reported, for completeness, in Table 2. From this graph we conclude that the S_{conf} parameter can be effectively used as a metric to relate very different measurement techniques aimed at detecting particle diffusion in heterogeneous environments. Moreover, it is evident how the simulation of compartmentalized diffusion we undertook is able to closely match experimental detection that we analysed without prior assumptions of the model that would describe our data (see Materials and Methods). This may serve as an indication that the cellular membrane is indeed a compartmentalized environment, whose physical characteristics may be effectively explored.

Conclusions

In this work, we have presented an example of how ISCAT microscopy can be applied to the study of the dynamics of lipids on the cellular membrane through SPT. We adopted a simple labelling protocol, adjusted from [51], which can be readily adopted for future similar studies. However, the novelty of this study lies mainly in the analysis protocol adopted, which can be thought as a development on the pipeline presented in [47]. The data analysis methodology we presented here is based on the observation of the apparent diffusion coefficient $D_{app}(t_n)$, a quantity derived directly from the raw mean squared displacements (MSD) (Eq. 3). This variable provides a more readily interpreted physical quantity, as it allows a direct comparison between the behaviour of the diffusion coefficient against time across trajectories or samples. The data analysis through model fitting was then performed in a way that minimizes bias and assumptions, by adopting a set of models, and choosing the most appropriate one through a combination of goodness-of-fit tests and BIC minimization. This modified approach establishes a robust statistical methodology for determining the most likely type of diffusive motion mode, from a particular given set of evaluated motion models, albeit it cannot be used to make any judgement about ruling out the appropriateness of non-tested models. Finally, we point out that our fitting routine has employed the localization uncertainty as a free parameter of the fits to the trajectory data of diffusing lipids. This has allowed us to accurately estimate the of magnitude of the dynamic localization uncertainty as opposed to the commonly used much smaller static localization uncertainty that is in contrast obtained from immobilized gold particles. This has enabled us to accurately assess the magnitude of the localization uncertainty corrected magnitude of the $D(t_n)$ at the very first time points.

From the formulation of the diffusive motion models adopted (Eq. 5-9), we have been able to directly address the physical properties underlying the plasma membrane

environment, effectively using the tracked particles as a probe. Initially, we collected the $D_{app}(t_n)$ curves and averaged them according to the tag size (Ø20nm or Ø40nm gold nanoparticles). From the results of the data analysis on the ensemble averaged $D_{app}(t_n)$ data, the compartmentalized diffusion model (with non-zero localization uncertainty) emerges as the most likely of the models considered. This model (Eq. 8) is representative of an underlying environment where the diffusing particles are divided into compartments surrounded by a partially permeable barrier. Thus, the movement of the particles can be separated into a short-range, time-decaying component, typical of the faster motion inside the compartments, and a long-range, time-invariant component that is representative of the slower motion between compartments. From the fit parameters thus extracted, the most noticeable effect was that the gold nanoparticle size apparently only influences the long-range, time-invariant, diffusion coefficient component of the tracked particles, without large influences on the diffusion mode itself. This is further corroborated by the values obtained for other parameters, such as the average compartment size L, and the short-range, time-decaying diffusion coefficient component D_μ, which are largely invariant with respect the gold nanoparticle size. This translates in the fact that, overall, the diffusion coefficient D(t) at all time scales is noticeably lowered when larger tags are adopted. Apart from the ensemble average analysis, we have further refined the analysis by classifying the single trajectories according to the most appropriate model that describe their motion. This allows us to gain more insights into the heterogeneity of behaviour of the target molecules, by focusing on a population of interest. While the distribution of fit parameters is understandably quite large, due to fluctuations in the highly variable environment of the cell membrane, it nevertheless confirms our previous findings. Moreover, it provides a viable avenue to investigate trajectory populations with common diffusion mode, rather than just diffusivity, thereby increasing the specificity of the analysis protocol we here presented.

Another strategy we employed to further our understanding of the plasma membrane environment is to compare the experimental data to ensembles of simulated trajectories. We employed a simulation framework in which a two-dimensional space is corralled into compartments of fixed average size L_S and random shape, over which particles diffuse at a fixed rate D_S and have a probability of "hopping" from one compartment to the other P_{Hop}. This is effectively a direct implementation of the "hop" diffusion model first proposed by Kusumi and co-workers [13], [14]. By running the simulations with various combination of the aforementioned parameters (and additionally, of a simulated localization uncertainty δ_S), we were able to obtain a set of trajectories which closely reconstructs the $D_{app}(t_n)$ data calculated from experimental data, both for the ensemble average of all trajectories, and for the subpopulation diffusing by compartmentalized diffusion. This result confirms the compartmentalization of the cellular membrane in semi-permeable corrals, and of the analysis methodology thus far employed. One important observation from our study is that the magnitude of the short-range, time-decaying diffusive component D_μ, for both tag species, is on the same order of magnitude as the diffusion coefficient of the long-range, time-independent component D_M. This is in stark contrast with similar observations made in the past [13], [14], which have been interpreted to be consistent with a much faster microscopic diffusion rate (5-8μm^2/s) at short time ranges, albeit at faster frame rates (40-50kHz), and

using a piece-wise analysis strategy, where the first points of the MSD curve where analysed separately from the rest. A distinguishing difference between these studies is, however, that while we have employed the dynamic localization uncertainty to minimize artefacts thereof, the previous studies by Kusumi et al. have instead relied on the use of the much lower static localization uncertainty. Another finding derived from matching simulations to the experimental data, is that another effect of adopting large gold nanoparticles as tags results in lowered P_{Hop}, an effect to be taken into account when approaching the study of compartmentalized surface such as cellular membranes.

The simulation framework we applied here also allows us to view this experiment in a wider context, involving more studies and data from comparable experiments [47], [48], [65]. We defined a parameter, called confinement strength (S_{conf}) as the ratio between the intra-compartmental diffusion coefficient, D_0, and the inter-compartmental diffusion coefficient, D_∞. Using this parameter, we were able to correlate the results obtained with other similar diffusivity measurements in different cell lines, conditions and techniques, to the sets of simulated trajectories generated for this work. A clear pattern emerges, correlating S_{conf} with the hopping probability of the simulated particles. Although the model needs to be refined in order to attain wider applicability, it retains the potential to be a defining feature for future plasma membrane diffusivity experiments, being technique-agnostic and providing an interesting descriptor for the physical characteristics of the cell membrane environment.

Acknowledgements

The authors greatly acknowledge the Engineering and Physical Sciences Research Council (EPSRC) and Medical Research Council (MRC) for supporting the DPhil project of FR within the Oxford-Nottingham Biomedical Imaging Centre of Doctoral Training (ONBI-CDT) (Grant No. EP/L016052/1). Further, we acknowledge support by the EPA Cephalosporin Fund (Bio-ISCAT project), the MRC (Grant No. MC_UU_12010/unit programs G0902418 and MC_UU_12025), the Wellcome Trust (Grant No. 104924/14/Z/14 and Strategic Award 091911 (Micron)), MRC/BBSRC/EPSRC (Grant No. MR/K01577X/1), the Wolfson Foundation (for initial funding of the Wolfson Imaging Centre Oxford), and the John Fell Fund. The authors would like to acknowledge the support of Dr. Erdinc Sezgin and Dr. Dilip Shrestha for their scientific advice, and the Kukura Group (Oxford University) for the technical support in the initial phases of microscope development.

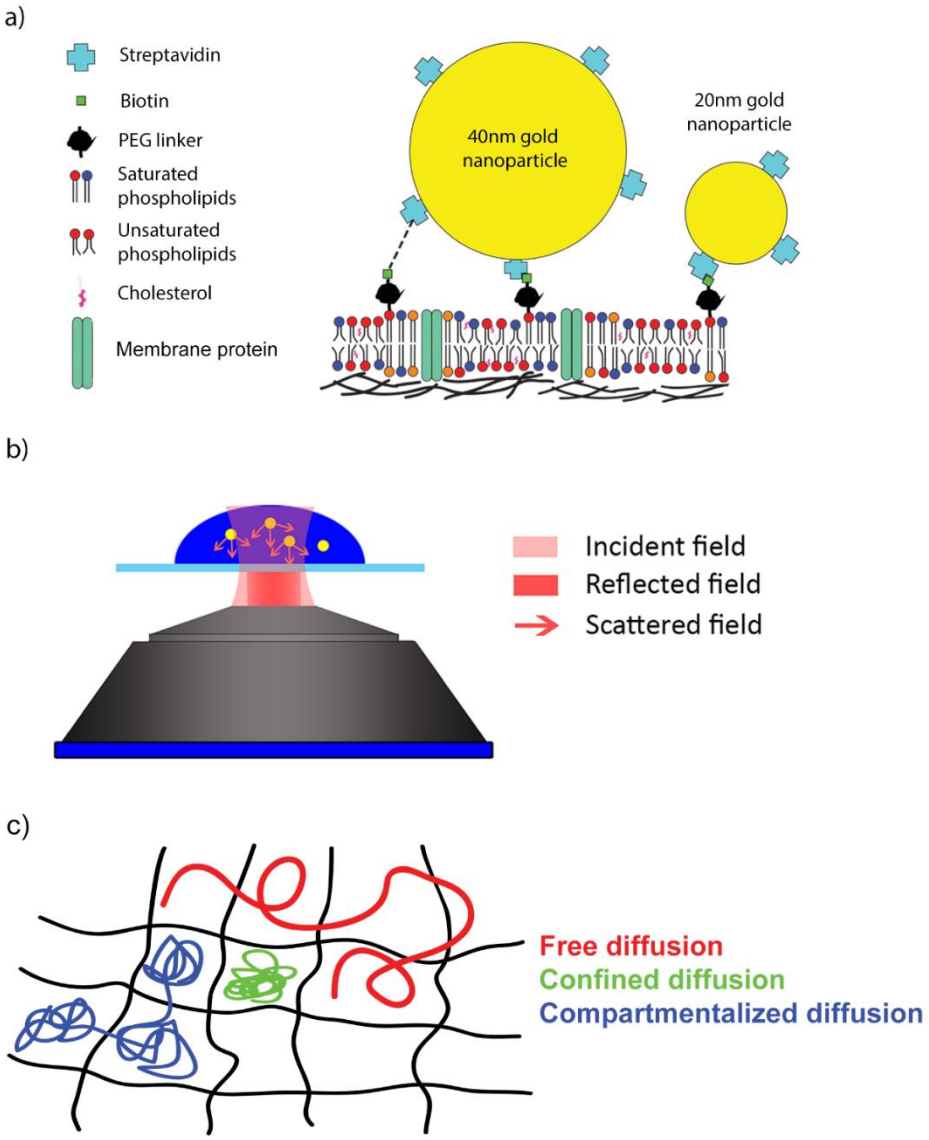

Figure 1 – Outline of fundamental concepts. a) Scheme for the labelling of the cell surface. The scattering tags, gold nanoparticles of two different diameters (20nm and 40nm) target the biotinylated lipids inserted in the cellular membrane, owing to their streptavidin coating. b) Fundamental principle of ISCAT microscopy: the incident field reaches the sample through the objective lens, whereby it is scattered by the sample. The component of incident light reflected by the glass-sample interface (the "reflected field") and the codirectional component of the scattered field are collected by the same objective, and generate an interference figure on the detector camera. c) Hypothesized diffusion modes on the surface of the cell membrane. The underlying actin cytoskeleton (in black) creates a meshwork of confinement regions on which the constituents of the cellular membrane diffuse. The diffusing molecules may not feel the presence of the boundaries, thereby diffusing in Brownian, or free, fashion, or may be affected in different degrees, by having their movement restricted to a limited region (confined diffusion), or by diffusing from one compartment to the other, with transient confinements (compartmentalized diffusion).

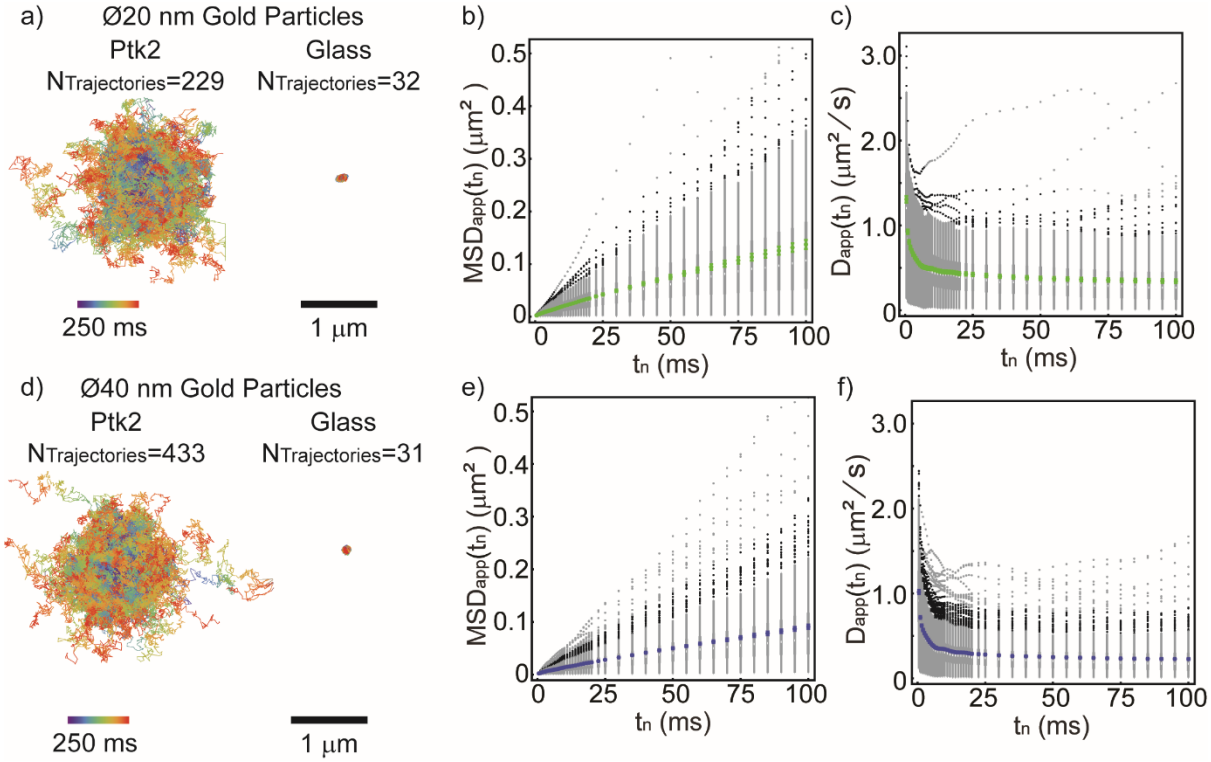

Figure 2. Experimental ISCAT tracking data. a) Superimposed trajectories from time-lapse image acquisitions of (left) diffusing DSPE-PEG(2000)-Biotin lipid analogues labelled with Ø20 nm diameter, streptavidin-coated gold nanoparticles, and (right) the same gold nanoparticles immobilized on glass (acquisition frame rate = 2kHz). All trajectories were truncated to 250ms (n=500 displacements) long segments, re-mapped to start at the same position. The color scale indicates the time of each localization (blue to red). b) Conventional, camera blur-corrected MSD_{app} data for all trajectories in a). Data are shown in box-and-whisker format. Also shown (green) is the ensemble average MSD curve with error bars corresponding to the standard error of the mean (s.e.m.). c) Same data as in b) in the $D_{app}(t_n)=MSD_{app}(t_n)/(4t_n)$ format. d-f) show the same plots as a-c), but where the probe is the Ø40nm streptavidin-coated gold nanoparticle and where ensemble average $MSD_{app}(t_n)$ and $D_{app}(t_n)$ curves are shown in blue.

Figure 3. Ensemble Average Trajectory Analysis

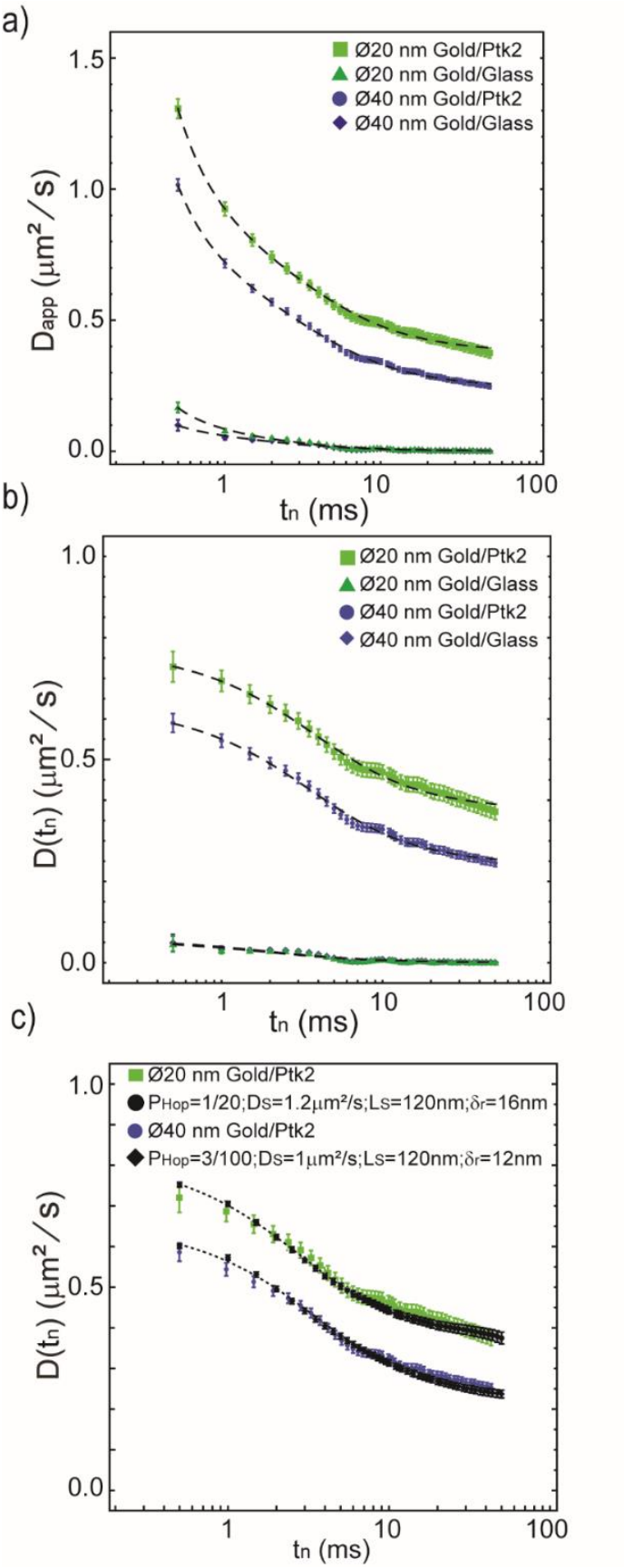

Figure 3. Ensemble average analysis results for diffusing streptavidin-coated gold nanoparticles-tagged DSPE-PEG(2000)-Biotin lipid analogues on PtK2 cell membrane at different time ranges a) Time dependence of the ensemble average of $D_{app}(t_n)$) of gold nanoparticles-tagged lipids on PtK2 cells for labelling with Ø20 nm gold nanoparticles (green squares) and Ø40 nm gold nanoparticles (blue circles), and the same size nanoparticles immobilized on glass (Ø20 nm (green triangles); Ø40 nm (blue diamonds)). The most likely model of diffusion was compartmentalized diffusion with localization uncertainty for both nanoparticle sizes, and confined diffusion for nanoparticles immobilized on glass (dashed lines). The fit results are shown in Supplementary Tables 4-7. For comparison, the conventional $MSD_{app}(t_n)$ plot format for the same data is shown in Supplementary Fig. 7a. b) Same data shown in a), but where the effect of the localization uncertainty has been subtracted. Estimation of the localization uncertainty is performed by using the fit parameters to the most likely model in each case (panel a, dashed lines). The corresponding $MSD(t_n)$ data are shown in Supplementary Fig. 7b. c) The $D_{app}(t_n)$ data presented in panel b) are overlayed with the corresponding data obtained from analysing simulated trajectories using the following parameters: P_{Hop}=1/20, D_S=1.2 $\mu m^2/s$, L_S=120 nm, and $\delta_{r\,S}$=16 nm (black open circles) and P_{Hop}=3/100, D_S=1.0 $\mu m^2/s$, L_S=120 nm, and $\delta_{r\,S}$=12 nm (black open diamonds). The superimposed simulated trajectories are plotted in Supplementary Figure 8.

Figure 4. Average Trajectory Analysis Parameters

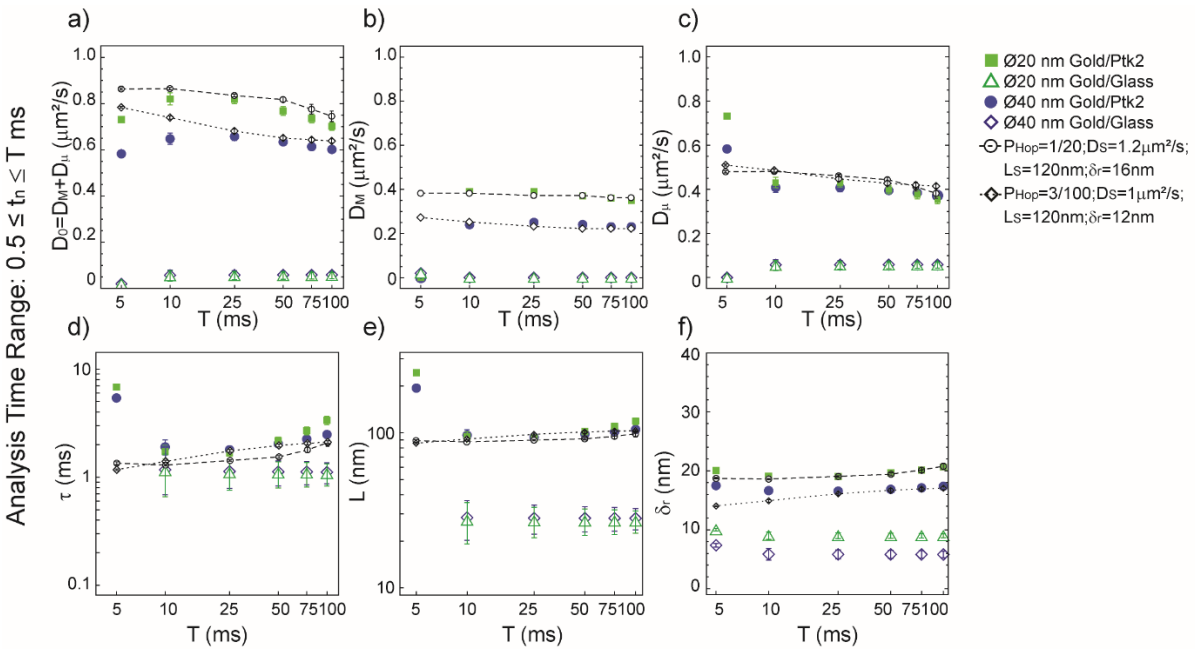

Figure 4. Ensemble average analysis results for diffusing streptavidin-coated gold nanoparticles-tagged DSPE-PEG(2000)-Biotin lipid analogues on PtK2 cell membrane at different time ranges a–f) Results for the fit parameters to the ensemble average $D_{app}(t_n)$ data in different time intervals ($0.5 \leq t_n \leq T$ ms with T= 5, 10, 25, 50, 75, and 100 ms). The color scheme is for labelling with Ø20 nm gold nanoparticles (green closed squares) and Ø40 nm gold nanoparticles (blue closed circles), and the same size nanoparticles immobilized on glass (Ø20 nm (green open triangles); Ø40 nm (blue open diamonds)). The parameters shown here are: a) the unhindered diffusion coefficient at time t=0, $D_0 = D_M + D_\mu$, b) Time-independent ("free") diffusion coefficient D_M, c) the time-dependent ("confined") diffusion coefficient D_μ, d) the average decay time τ for the microscopic diffusive component D_μ, e) the confinement size $L=(12\ D_\mu\tau)^{1/2}$, and f) the localization uncertainty δ_r. Also shown are the corresponding fit parameters from the ensemble average analysis of the matching simulated trajectory for tagging with Ø20 nm gold particles (black open circles linked by dashed black lines) and Ø40 nm gold particles (black open diamonds linked by dotted black lines).

Figure 5. Single Trajectory Analysis Results

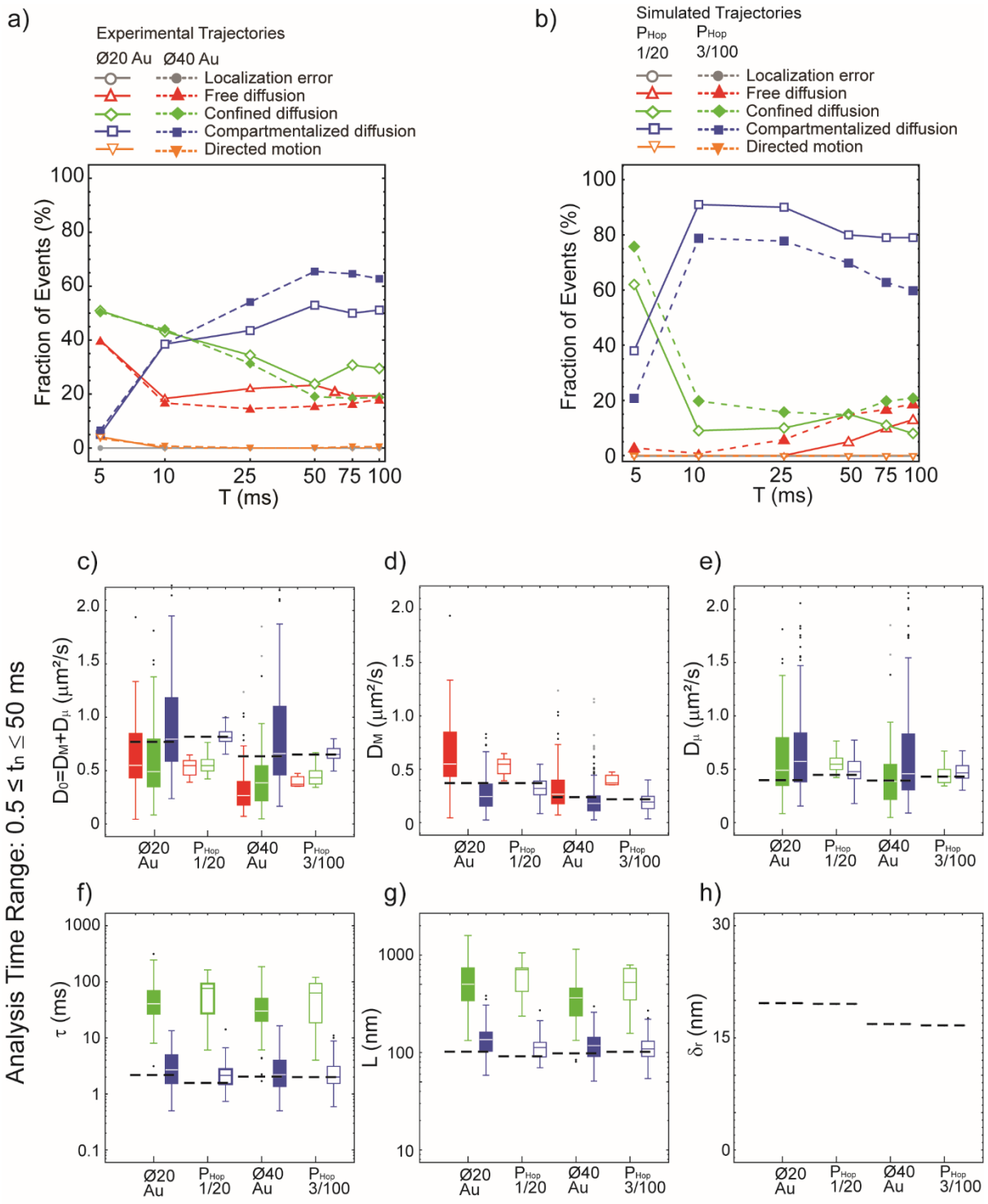

Figure 5. Single Trajectory Analysis Results. a) Relative fractions of the trajectories by most likely diffusion model at different analysis time ranges, for labelling with Ø20 nm gold nanoparticles (open markers, solid line) and Ø40 nm gold nanoparticles (closed markers,

dashed line). b) Relative fractions of simulated trajectories best described by each diffusion model at different analysis time ranges ($0.5 \leq t_n \leq T$ ms with T= 5, 10, 25, 50, 75, and 100 ms). Trajectories of single particle diffusing in a lattice were simulated using $P_{hop} = 1/20$ (open markers, solid line) and $P_{hop} = 3/100$ (closed markers, dashed line). c-h) Comparison of the distribution of fit parameters from the single trajectory analysis, for an analysis time range of $0.5 \leq t_n \leq 50$ ms, for experimental data (filled boxes) and matching simulated trajectory data (hollow boxes). The color scheme for the boxes is the same as the diffusion modes color scheme in panels a-b). The graphs report the distribution of: c) the unhindered diffusion coefficient at time t=0, $D_0 = D_M + D_\mu$; d) the macroscopic, diffusion coefficient D_M; e) the microscopic diffusion coefficient D_μ; f) the average decay time $\tau=L^2/(12\ D_\mu)$ for the microscopic diffusive component D_μ; g) the confinement size $L=(12\ D_\mu\tau)^{1/2}$, and h) the localization uncertainty δ_r. This last panel highlights the fact that the localization uncertainty has been fixed on the value obtained for the ensemble average analysis for all trajectories, simulated and detected. In all panels, the dashed lines represent the average values of the corresponding parameters as determined from the ensemble average analysis at the same analysis time range.

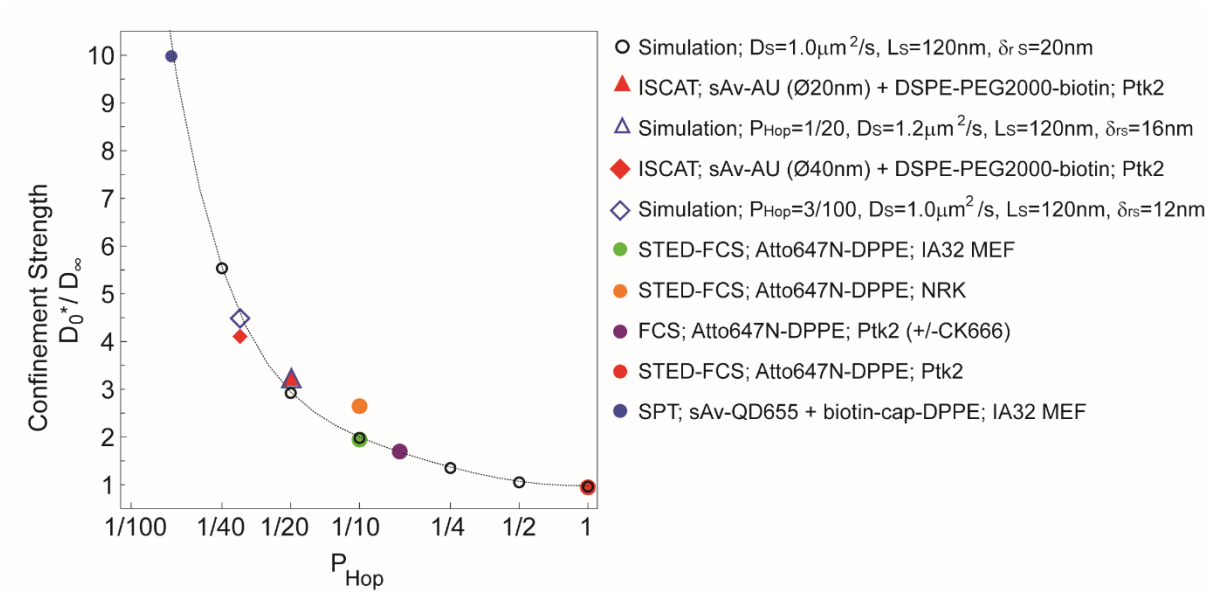

Figure 6. Comparison of ISCAT experimental results to our previous lateral diffusion in plasma membrane of live cells by STED-FCS, FCS, and SPT. To put the results from this study into context with previous related studies, we have plotted the modified confinement strength, D_0^*/D_∞, as determined by comparative analysis of simulated trajectory data for compartmentalized diffusion, versus the hopping probability, P_{Hop}, for data as indicated in the Figure legend.

Table 1 – Summary of trajectories analysed in this study. $N_{\mathrm{Trajectories}}$ refers to the total number of trajectories per sample, while $N^{500}_{\mathrm{Trajectories}}$ refers to the corresponding number of 500 localization-long segments extracted

Probe	$N_{Trajectories}$	Trajectory Length (±s.t.d.)	$N^{500}_{Trajectories}$
DSPE -PEG2000-biotin / sAv-Au (Ø20nm) on Ptk2 cells	92	1430 ± 970	229
DSPE-PEG2000-Biotin / sAv-Au (Ø40nm) on Ptk2 cells	165	1510 ± 1040	433
sAv-Au (Ø20nm) immobilized on glass	4	4000 ± 0	32
sAv-Au (Ø40nm) immobilized on glass	4	4000 ± 1	31

Table 2 – Comparison of the values for the Diffusion coefficients, confinement strength and other relevant parameters obtained from the diffusion experiments and simulation from this study, with those obtained from related literature.

Method	Probe	Cell line	Analysis	Analysis Time Range	D_0 ($\mu m^2/s$)	D_∞ ($\mu m^2/s$)	L (nm)	$S_{Conf}= D_0/D_\infty$	$\tau_{Conf}=L^2/(4D_\infty)$ (ms)
ISCAT[1]	biotin-PEG2000-DSPE / sAv-Au (Ø20nm)	Ptk2	Ensemble Average	$0.5 \leq t_n \leq 50$ ms	0.77±0.02	0.37±0.00	100±5	2.1±0.1	6.8±0.4
			Compartmentalized Diffusion Subset (119/225 trajectories)		0.95±0.05	0.28±0.02	145±5	3.4±0.2	19±1
Simulation P_{Hop}=0.05; D_S=1.2 $\mu m^2/s$; L_S=120 nm; δ_{r_S}=16 nm[1]	-	-	Ensemble Average	$0.5 \leq t_n \leq 50$ ms	0.82±0.02	0.37±0.00	92±1.7	2.2±0.1	5.7±0.1
			Compartmentalized Diffusion Subset (70/100 trajectories)		0.82±0.01	0.32±0.01	115±4	2.6±0.1	10±0.7
ISCAT[1]	biotin-PEG2000-DSPE / sAv-Au (Ø40nm)	Ptk2	Ensemble Average	$0.5 \leq t_n \leq 50$ ms	0.63±0.02	0.24±0.00	98±3.5	2.6±0.1	10±0.5
			Compartmentalized Diffusion Subset (283/422 trajectories)		0.82±0.03	0.21±0.01	122±2	3.9 ± 0.2	18±1
Simulation P_{Hop}=0.03; D_S=1.0 $\mu m^2/s$; L_S=120 nm; δ_{r_S}=12 nm[1]	-	-	Ensemble Average	$0.5 \leq t_n \leq 50$ ms	0.65±0.02	0.22±0.00	100±2.1	3.0±0.1	11±0.3
			Compartmentalized Diffusion Subset (80/100 trajectories)		0.66±0.01	0.19±0.01	117±4	3.5±0.1	18±1

[1] Data featured in this work

STED-FCS[2]	Atto647N-DPPE	IA32 MEF (Ink4a/Arf (-/-))	Ensemble Average	$\approx 0.5 \leq t_D \leq \approx 30$ ms	0.80±0.03	≈ 0.4	150±12	≈ 2.0 [3]	14±2
STED-FCS[Error! Bookmark not defined.]	Atto647N-DPPE	NRK	Ensemble Average	$\approx 0.5 \leq t_D \leq \approx 30$ ms	0.80±0.03	≈ 0.3	80±8	≈ 2.7 [3]	5.3±0.5
FCS (+/-CK-666)[2]	Atto647N-DPPE	Ptk2	Ensemble Average	$\approx 0.5 \leq t_D \leq \approx 30$ ms	≈ 0.70 (+CK666)	≈ 0.40 (-CK666)	N/A	≈ 1.8 [4]	N/A
STED-FCS [5]	Atto647N-DPPE	Ptk2	Ensemble Average	$\approx 0.5 \leq t_D \leq \approx 30$ ms	≈ 0.40	≈ 0.40	N/A	≈ 1.0 [3]	0
SPT [6]	biotin-cap-DPPE / sAv-QD655	IA32 MEF (Ink4a/Arf (-/-))	Ensemble Average	$\approx 0.6 \leq t_n \leq 50$ ms	0.78±0.06	0.078±0.001	110±2	10±0.8 [3]	39 ± 1

[2] Data featured in [48]

[3] For STED-FCS measurements, D_0 is the diffusion coefficient calculated from data acquired at the greatest available STED power (here corresponding to an approximate lateral resolution of 50 nm), whereas we have defined D_∞ as the diffusion coefficient calculated from data acquired at confocal lateral resolution (~250 nm). Thus the confinement strength, S_{Conf}, for STED-FCS is defined as $S_{Conf} = D_0/D_\infty = D_{STED}/D_{Confocal}$

[4] For conventional FCS measurements with and without Arp2/3 specific inhibitor CK-666, we have defined D_0 as the diffusion coefficient calculated from measurements in the presence of 100 µM CK-666, whereas D_∞ is the extracted diffusion coefficient for data acquired in the absence of CK-666. Thus the confinement strength, S_{Conf}, for FCS in this case is defined as $S_{Conf} = D_0/D_\infty = D_{Confocal}^{+CK666}/D_{Confocal}^{-CK666}$

[5] Data featured in [65]

[6] Data featured in [47]

References

[1] K. Simons and M. J. Gerl, "Revitalizing membrane rafts: New tools and insights," *Nat. Rev. Mol. Cell Biol.*, vol. 11, no. 10, pp. 688–699, 2010, doi: 10.1038/nrm2977.

[2] K. Jacobson, P. Liu, and B. C. Lagerholm, "The Lateral Organization and Mobility of Plasma Membrane Components," *Cell*, vol. 177, no. 4, pp. 806–819, 2019, doi: 10.1016/j.cell.2019.04.018.

[3] M. L. Kraft, "Plasma membrane organization and function: moving past lipid rafts.," *Mol. Biol. Cell*, vol. 24, no. 18, 2013, doi: 10.1091/mbc.E13-03-0165.

[4] C. Di Rienzo *et al.*, "Fast spatiotemporal correlation spectroscopy to determine protein lateral diffusion laws in live cell membranes," *Proc Natl Acad Sci U S A*, vol. 110, no. 30, pp. 12307–12312, 2013, doi: 10.1073/pnas.1222097110.

[5] G. L. Nicolson, "The Fluid - Mosaic Model of Membrane Structure: Still relevant to understanding the structure, function and dynamics of biological membranes after more than 40 years," *Biochim. Biophys. Acta - Biomembr.*, vol. 1838, no. 6, pp. 1451–1466, 2014, doi: 10.1016/j.bbamem.2013.10.019.

[6] A. Kusumi *et al.*, "Dynamic Organizing Principles of the Plasma Membrane that Regulate Signal Transduction: Commemorating the Fortieth Anniversary of Singer and Nicolson's Fluid-Mosaic Model," *Annu. Rev. Cell Dev. Biol.*, vol. 28, no. 1, pp. 215–250, Nov. 2012, doi: 10.1146/annurev-cellbio-100809-151736.

[7] J. Perrin, *Brownian Movement and Molecular Reality*. London: Taylor & Francis, 1910.

[8] N. Hiramoto-Yamaki *et al.*, "Ultrafast Diffusion of a Fluorescent Cholesterol Analog in Compartmentalized Plasma Membranes," *Traffic*, vol. 15, no. 6, pp. 583–612, 2014, doi: 10.1111/tra.12163.

[9] R. Simson, E. D. Sheets, and K. Jacobson, "Detection of temporary lateral confinement of membrane proteins using single-particle tracking analysis," *Biophys. J.*, vol. 52, no. June, pp. 989–993, 1995, doi: 10.1016/S0006-3495(95)79972-6.

[10] F. Balzarotti *et al.*, "Nanometer resolution imaging and tracking of fluorescent molecules with minimal photon fluxes," *Science (80-.).*, vol. 355, no. 6325, pp. 606–612, Feb. 2017, doi: 10.1126/science.aak9913.

[11] Y. Eilers, H. Ta, K. C. Gwosch, F. Balzarotti, and S. W. Hell, "MINFLUX monitors rapid molecular jumps with superior spatiotemporal resolution," *Proc. Natl. Acad. Sci.*, vol. 115, no. 24, pp. 6117–6122, 2018, doi: 10.1073/pnas.1801672115.

[12] Y. M. Umemura, M. Vrljic, S. Y. Nishimura, T. K. Fujiwara, K. Suzuki, and A. Kusumi, "Both MHC class II and its GPI-anchored form undergo hop diffusion as observed by single-molecule tracking," *Biophys. J.*, vol. 95, no. 1, pp. 435–450, 2008, doi: 10.1529/biophysj.107.123018.

[13] K. Murase *et al.*, "Ultrafine Membrane Compartments for Molecular Diffusion as

Revealed by Single Molecule Techniques," *Biophys. J.*, vol. 86, no. 6, pp. 4075–4093, Jun. 2004, doi: 10.1529/biophysj.103.035717.

[14] T. Fujiwara, K. Ritchie, H. Murakoshi, K. Jacobson, and A. Kusumi, "Phospholipids undergo hop diffusion in compartmentalized cell membrane," *J. Cell Biol.*, vol. 157, no. 6, pp. 1071–1082, Jun. 2002, doi: 10.1083/jcb.200202050.

[15] H. Geerts *et al.*, "Nanovid tracking: a new automatic method for the study of mobility in living cells based on colloidal gold and video microscopy," *Biophys. J.*, vol. 52, no. 5, pp. 775–782, 1987, doi: 10.1016/S0006-3495(87)83271-X.

[16] M. De Brabander, R. Nuydens, H. Geerts, and C. R. Hopkins, "Dynamic behavior of the transferrin receptor followed in living epidermoid carcinoma (A431) cells with nanovid microscopy.," *Cell Motil. Cytoskeleton*, vol. 9, no. 1, pp. 30–47, 1988, doi: 10.1002/cm.970090105.

[17] M. De Brabander, R. Nuydens, A. Ishihara, B. Holifield, K. Jacobson, and H. Geerts, "Lateral diffusion and retrograde movements of individual cell surface components on single motile cells observed with nanovid microscopy," *J. Cell Biol.*, vol. 112, no. 1, pp. 111–124, 1991, doi: 10.1083/jcb.112.1.111.

[18] A. S. G. Curtis, "A Study by Interference Reflection Microscopy," *J. Cell Biol.*, vol. 20, no. 1, pp. 199–215, 1964, doi: 10.1083/jcb.20.2.199.

[19] G. A. Dunn, "Quantitative Interference Microscopy," in *New Techniques of Optical Microscopy and Microspectroscopy*, R. J. Cherry, Ed. London: Macmillan Education UK, 1991, pp. 91–118.

[20] J. Ortega-Arroyo *et al.*, "Label-Free, All-Optical Detection, Imaging, and Tracking of a Single Protein," *Nano Lett.*, vol. 14, no. 4, pp. 2065–2070, Apr. 2014, doi: 10.1021/nl500234t.

[21] K. M. Spillane *et al.*, "High-Speed Single-Particle Tracking of GM1 in Model Membranes Reveals Anomalous Diffusion due to Interleaflet Coupling and Molecular Pinning.," *Nano Lett.*, vol. 14, no. 9, pp. 5390–7, 2014, doi: 10.1021/nl502536u.

[22] R. W. Taylor, R. G. Mahmoodabadi, V. Rauschenberger, A. Giessl, A. Schambony, and V. Sandoghdar, "Interferometric scattering microscopy reveals microsecond nanoscopic protein motion on a live cell membrane," *bioRxiv*, vol. 13, no. July, p. DOI:10.1101/401133, 2018, doi: 10.1101/401133.

[23] C.-L. Hsieh, "Label-free, ultrasensitive, ultrahigh-speed scattering-based interferometric imaging," *Opt. Commun.*, vol. 422, no. December 2017, pp. 69–74, 2018, doi: 10.1016/j.optcom.2018.02.058.

[24] Y. F. Huang, G. Y. Zhuo, C. Y. Chou, C. H. Lin, and C.-L. Hsieh, "Label-free, ultrahigh-speed, 3D observation of bidirectional and correlated intracellular cargo transport by coherent brightfield microscopy," *Nanoscale*, vol. 9, no. 19, pp. 6567–6574, 2017, doi: 10.1039/c7nr00604g.

[25] G. de Wit, D. Albrecht, H. Ewers, and P. Kukura, "Revealing Compartmentalized Diffusion in Living Cells with Interferometric Scattering Microscopy," *Biophys. J.*, vol.

114, no. 12, pp. 2945–2950, Jun. 2018, doi: 10.1016/j.bpj.2018.05.007.

[26] K. Lindfors, T. Kalkbrenner, P. Stoller, and V. Sandoghdar, “Detection and spectroscopy of gold nanoparticles using supercontinuum white light confocal microscopy,” *Phys. Rev. Lett.*, vol. 93, no. 3, pp. 037401–1, Jul. 2004, doi: 10.1103/PhysRevLett.93.037401.

[27] Y. F. Huang, G. Y. Zhuo, C. Y. Chou, C. H. Lin, W. Chang, and C.-L. Hsieh, “Coherent Brightfield Microscopy Provides the Spatiotemporal Resolution to Study Early Stage Viral Infection in Live Cells,” *ACS Nano*, vol. 11, no. 3, pp. 2575–2585, 2017, doi: 10.1021/acsnano.6b05601.

[28] R. W. Taylor and V. Sandoghdar, “Interferometric Scattering (iSCAT) Microscopy & Related Techniques,” *ArXiv*, pp. 1–42, Dec. 2018, doi: arXiv:1812.10765v1.

[29] G. de Wit, J. S. H. Danial, P. Kukura, and M. I. Wallace, “Dynamic label-free imaging of lipid nanodomains,” *Proc. Natl. Acad. Sci.*, vol. 112, no. 40, pp. 12299–12303, 2015, doi: 10.1073/pnas.1508483112.

[30] L. Tala, A. Fineberg, P. Kukura, and A. Persat, “Label-free visualization of type IV pili dynamics by interferometric scattering microscopy,” *bioRxiv*, p. 298562, Apr. 2018, doi: 10.1101/298562.

[31] M. P. Clausen and B. C. Lagerholm, “The Probe Rules in Single Particle Tracking,” *Curr. Protein Pept. Sci.*, vol. 12, no. 8, pp. 699–713, Dec. 2011, doi: 10.2174/138920311798841672.

[32] F. Reina *et al.*, “Complementary studies of lipid membrane dynamics using iSCAT and super-resolved fluorescence correlation spectroscopy,” *J. Phys. D. Appl. Phys.*, vol. 51, no. 23, p. 235401, Jun. 2018, doi: 10.1088/1361-6463/aac04f.

[33] C.-L. Hsieh, S. Spindler, J. Ehrig, and V. Sandoghdar, “Tracking single particles on supported lipid membranes: Multimobility diffusion and nanoscopic confinement,” *J. Phys. Chem. B*, vol. 118, no. 6, pp. 1545–1554, Feb. 2014, doi: 10.1021/jp412203t.

[34] J. Andrecka, J. Ortega-Arroyo, and P. Kukura, “Direct observation and control of Supported lipid bilayer formation with interferometric scattering Microscopy,” *ACS Nano*, vol. 7, no. 12, pp. 10662–10670, 2013, doi: 10.1021/nn403367c.

[35] M. P. McDonald *et al.*, “Visualizing Single-Cell Secretion Dynamics with Single-Protein Sensitivity,” *Nano Lett.*, vol. 18, no. 1, pp. 513–519, 2018, doi: 10.1021/acs.nanolett.7b04494.

[36] S. Spindler *et al.*, “Visualization of lipids and proteins at high spatial and temporal resolution via interferometric scattering (iSCAT) microscopy,” *J. Phys. D. Appl. Phys.*, vol. 49, no. 27, p. 274002, 2016, doi: 10.1088/0022-3727/49/27/274002.

[37] M. Piliarik and V. Sandoghdar, “Direct optical sensing of single unlabelled proteins and super-resolution imaging of their binding sites,” *Nat. Commun.*, vol. 5, pp. 1–8, 2014, doi: 10.1038/ncomms5495.

[38] A. Einstein, *Investigations on the Theory of the Brownian Movement*. Dover Publications, 1956.

[39] M. von Smoluchowski, “Zur kinetischen Theorie der Brownschen Molekularbewegung und der Suspensionen,” *Ann. Phys.*, vol. 326, no. 14, pp. 756–780, 1906, doi: 10.1002/andp.19063261405.

[40] R. Kubo, “The fluctuation-dissipation theorem,” *Reports Prog. Phys.*, vol. 29, no. 1, p. 306, Jan. 1966, doi: 10.1088/0034-4885/29/1/306.

[41] X. Michalet, “Mean square displacement analysis of single-particle trajectories with localization error: Brownian motion in an isotropic medium,” *Phys. Rev. E*, vol. 82, no. 4, p. 041914, Oct. 2010, doi: 10.1103/PhysRevE.82.041914.

[42] T. Savin and P. S. Doyle, “Static and Dynamic Errors in Particle Tracking Microrheology,” *Biophys. J.*, vol. 88, no. 1, pp. 623–638, Jan. 2005, doi: 10.1529/biophysj.104.042457.

[43] D. Montiel, H. Cang, and H. Yang, “Quantitative Characterization of Changes in Dynamical Behavior for Single-Particle Tracking Studies †,” *J. Phys. Chem. B*, vol. 110, no. 40, pp. 19763–19770, Oct. 2006, doi: 10.1021/jp062024j.

[44] M. Goulian and S. M. Simon, “Tracking Single Proteins within Cells,” *Biophys. J.*, vol. 79, no. 4, pp. 2188–2198, Oct. 2000, doi: 10.1016/S0006-3495(00)76467-8.

[45] D. S. Martin, M. B. Forstner, and J. A. Käs, “Apparent subdiffusion inherent to single particle tracking,” *Biophys. J.*, vol. 83, no. 4, pp. 2109–2117, 2002, doi: 10.1016/S0006-3495(02)73971-4.

[46] J. Gelles, B. J. Schnapp, and M. P. Sheetz, “Tracking kinesin-driven movements with nanometre-scale precision,” *Nature*, vol. 331, no. 6155, pp. 450–453, Feb. 1988, doi: 10.1038/331450a0.

[47] B. C. Lagerholm, D. M. Andrade, M. P. Clausen, and C. Eggeling, “Convergence of lateral dynamic measurements in the plasma membrane of live cells from single particle tracking and STED-FCS,” *J. Phys. D. Appl. Phys.*, vol. 50, no. 6, p. 063001, 2017, doi: 10.1088/1361-6463/aa519e.

[48] D. M. Andrade *et al.*, “Cortical actin networks induce spatio-temporal confinement of phospholipids in the plasma membrane – a minimally invasive investigation by STED-FCS,” *Sci. Rep.*, vol. 5, no. May, p. 11454, 2015, doi: 10.1038/srep11454.

[49] M. Osborn, W. W. Franke, and K. Weber, “Visualization of a system of filaments 7-10 nm thick in cultured cells of an epithelioid line (Pt K2) by immunofluorescence microscopy.,” *Proc. Natl. Acad. Sci. U. S. A.*, vol. 74, no. 6, pp. 2490–4, Jun. 1977, doi: 10.1073/PNAS.74.6.2490.

[50] F. Schneider *et al.*, “Diffusion of lipids and GPI-anchored proteins in actin-free plasma membrane vesicles measured by STED-FCS,” *Mol. Biol. Cell*, vol. 28, no. 11, pp. 1507–1518, Apr. 2017, doi: 10.1091/mbc.E16-07-0536.

[51] E. Sezgin *et al.*, *Measuring nanoscale diffusion dynamics in cellular membranes with super-resolution STED–FCS*, vol. 14, no. 4. 2019.

[52] J. Ortega-Arroyo, D. Cole, and P. Kukura, “Interferometric scattering microscopy and its combination with single-molecule fluorescence imaging,” *Nat. Protoc.*, vol. 11, no.

4, pp. 617–633, 2016, doi: 10.1038/nprot.2016.022.

[53] Y. Sako and A. Kusumi, “Barriers for Lateral Diffusion of Transferrin Receptor in the Plasma Membrane as Characterized by Receptor Dragging by Laser Tweezers: Fence versus Tether,” Accessed: Dec. 19, 2017. [Online]. Available: http://jcb.rupress.org/content/jcb/129/6/1559.full.pdf.

[54] J. Schindelin *et al.*, “Fiji: An open-source platform for biological-image analysis,” *Nat. Methods*, vol. 9, no. 7, pp. 676–682, 2012, doi: 10.1038/nmeth.2019.

[55] X. Michalet and A. J. Berglund, “Optimal diffusion coefficient estimation in single-particle tracking,” *Phys. Rev. E - Stat. Nonlinear, Soft Matter Phys.*, vol. 85, no. 6, pp. 1–14, Jun. 2012, doi: 10.1103/PhysRevE.85.061916.

[56] S. Wieser, M. Moertelmaier, E. Fuertbauer, H. Stockinger, and G. J. Schütz, “(Un)confined diffusion of CD59 in the plasma membrane determined by high-resolution single molecule microscopy,” *Biophys. J.*, vol. 92, no. 10, pp. 3719–3728, 2007, doi: 10.1529/biophysj.106.095398.

[57] C. Dietrich, B. Yang, T. Fujiwara, A. Kusumi, and K. Jacobson, “Relationship of lipid rafts to transient confinement zones detected by single particle tracking,” *Biophys. J.*, vol. 82, no. 1, pp. 274–284, 2002, doi: 10.1016/S0006-3495(02)75393-9.

[58] C.-Y. Cheng, Y.-H. Liao, and C.-L. Hsieh, “High-speed imaging and tracking of very small single nanoparticles by contrast enhanced microscopy,” *Nanoscale*, vol. 18, no. 1, pp. 568–577, 2018, doi: 10.1039/C8NR06789A.

[59] K. P. Burnham and D. R. Anderson, *Model Selection and Multimodel Inference*, 2nd ed., vol. 172, no. 1. New York, NY: Springer New York, 2004.

[60] H. Qian, M. P. Sheetz, and E. L. Elson, “Single particle tracking. Analysis of diffusion and flow in two-dimensional systems,” *Biophys. J.*, vol. 60, no. 4, pp. 910–921, Oct. 1991, doi: 10.1016/S0006-3495(91)82125-7.

[61] A. Kusumi *et al.*, “Paradigm Shift of the Plasma Membrane Concept from the Two-Dimensional Continuum Fluid to the Partitioned Fluid: High-Speed Single-Molecule Tracking of Membrane Molecules,” *Annu. Rev. Biophys. Biomol. Struct.*, vol. 34, no. 1, pp. 351–378, 2005, doi: 10.1146/annurev.biophys.34.040204.144637.

[62] M. J. Saxton, “Single-particle tracking: The distribution of diffusion coefficients,” *Biophys. J.*, vol. 72, no. 4, pp. 1744–1753, 1997, doi: 10.1016/S0006-3495(97)78820-9.

[63] A. Kusumi, Y. Sako, and M. Yamamoto, “Confined lateral diffusion of membrane receptors as studied by single particle tracking (nanovid microscopy). Effects of calcium-induced differentiation in cultured epithelial cells,” *Biophys. J.*, vol. 65, no. 5, pp. 2021–2040, 1993, doi: 10.1016/S0006-3495(93)81253-0.

[64] Y. Sako and A. Kusumi, “Barriers for lateral diffusion of transferrin receptor in the plasma membrane as characterized by receptor dragging by laser tweezers: fence versus tether.,” *J. Cell Biol.*, vol. 129, no. 6, pp. 1559–1574, Jun. 1995, doi: 10.1083/jcb.129.6.1559.

[65] C. Eggeling *et al.*, “Direct observation of the nanoscale dynamics of membrane lipids in a living cell.,” *Nature*, vol. 457, no. 7233, pp. 1159–62, 2009, doi: 10.1038/nature07596.

[66] M. P. Clausen, E. C. Arnspang, B. Ballou, J. E. Bear, and B. C. Lagerholm, “Simultaneous multi-species tracking in live cells with quantum dot conjugates,” *PLoS One*, vol. 9, no. 6, p. e97671, Jun. 2014, doi: 10.1371/journal.pone.0097671.